AD-A073 385 AUBURN UNIV ALA DEPT OF PHYSICS F/G 20/5
NUCLEAR PUMPED LASERS,(U)
JUL 79 J R WILLIAMS, M J MONAHAN DAS660-77-C-0165
UNCLASSIFIED NL

1 OF 1
AD
A073385

END
DATE
FILMED
10-79
DDC

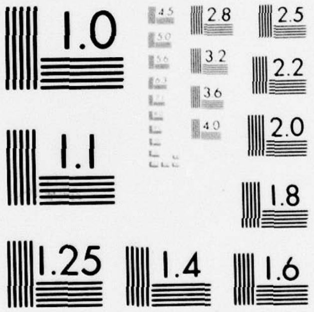
1.0
4.5
5.0
5.6
6.3
7.1
2.8
3.2
3.6
4.0
2.5
2.2
2.0
1.1
1.8
1.25
1.4
1.6

②

(6) NUCLEAR PUMPED LASERS,

Contract No. (15) DASG60-77-C-0165 new

U. S. Army Ballistic Missile Defense

Advanced Technology Center

Redstone Arsenal, AL

Submitted by

(10) J. R. Williams, M. J. Monahan~~, an~~d Q. C. Murphree

Physics Department, Auburn University, Auburn, AL 36830

(11) July~~, 1~~979 (12) 56p.

405 564

Final Report

Nuclear Pumped Lasers

Principal Investigator

John R. Williams
Physics Department
Auburn University
Auburn, AL 36830

Additional Investigators

M. J. Monahan and Q. C. Murphree
Physics Department
Auburn University
Auburn, AL 36830

Performance Period

September, 1977 - December, 1978

Submitted to

Mr. John Hagefstration
U. S. Army Ballistic Missile Advanced Technology Center
Redstone Arsenal, AL

Submitted from

Physics Department
Auburn University
Auburn, AL 36830

Date

1 July, 1979

ABSTRACT

A 3.5 MeV Dynamitron accelerator has been used to investigate low pressure mixtures ~~($P_{total} \approx 40$ torr)~~ of Kr-NF_3, Xe-NF_3, Kr-NF_3-UF_6, and Xe-NF_3-UF_6. The accelerator provides low intensity, guassian shaped, pulsed proton beams with FWHM pulse widths of 3 ns and repetition rates of 1 ~~μs~~ microsec to 32 ms. Emissions from the gas scintillation cell are observed with a single photon counting system. Under existing experimental conditions, the metastable reaction channel dominates the system kinetics, and analysis of experimental results gives formation rate constants, K_1, of 1.7×10^{-10} ~~cm^3~~ cc/sec and 5.5×10^{-11} ~~cm^3~~ cc/sec for the reactions

10 to the -11th power

$$Kr^* + NF_3 \xrightarrow{\overset{\text{To}}{K_1}} KrF^* + NF_2$$

10 to the -10th power

and

$$Xe^* + NF_3 \xrightarrow{\overset{\text{to}}{K_1}} XeF^* + NF_2,$$

respectively.

The results of absolute conversion efficiency measurements show the Xe-NF_3 system to be approximately an order of magnitude more efficient than the Kr-NF_3 system. The addition of approximately 0.75 torr of UF_6 to a 40/2 torr mixture of Kr/NF_3 reduces the 2487 Å emission by approximately 50%. A 50% reduction in the 3525 Å emission from a 40/4 torr mixture of Xe/NF_3 is observed when 2 torr of UF_6 are added. This reduction for the Xe-NF_3 system cannot be explained in terms of optical absorption by UF_6. The optical absorption cross section for UF_6 is approximately 6×10^{-21} cm^2 at 3525 Å, a low value compared with the cross section for most other wavelengths in the region 2000-4000 Å. Therefore, experimental results suggest strong collisional quenching of the XeF^* emission by small amounts of UF_6.

A

I. INTRODUCTION

Rare gas-halide laser systems have been studied extensively during the past few years, and recently, several survey articles concerning these systems have appeared in the literature.[1,2] These articles discuss the pumping of these systems by various methods. Specific discussions have been presented by Miley on the possibility of pumping these rare gas-halide systems with different types of nuclear reactors.[3]

A typical potential energy diagram[1] for a rare gas-halide molecule is shown in Figure 1. The ground state for all the rare gas-halide excimers is dissociative or very weakly bound, and this is the feature that makes them attractive as potential laser candiates. The upper laser level is generally ionic in character; however, this level can be formed through the ion or the metastable reaction channel, depending on the experimental conditions.

Two systems, KrF and XeF, have been investigated in the present study. The ground state of KrF can be represented by the solid curve in Figure 1 while the dotted curve represents the weakly bound ground state of XeF. The natural radiative lifetime for each of the upper laser levels has been reported as 6.8 ns [4] and 16 ns[1] for KrF^* and XeF^*, respectively. Rate constants for the collisional quenching of these levels by Kr, Xe, F_2, and NF_3 are given in references 5, 6, and 7. Velasco <u>et</u>. <u>al</u>. [8] have determined total quenching rate constants for the $Kr^*(^3P_2)$ and $Xe^*(^3P_2)$ metastable states in $Xe\text{-}F_2$, $Xe\text{-}NF_3$, $Kr\text{-}F_2$, and $Kr\text{-}NF_3$ mixtures.

In the present work, experiments have been performed to investigate the feasibility of using a Dynamitron accelerator [Section II (A)]

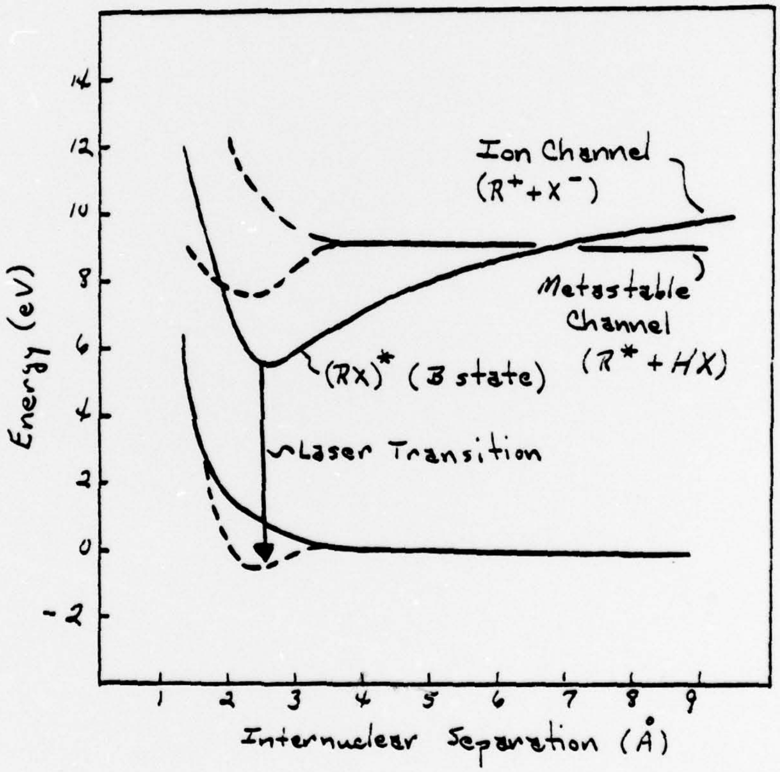

Figure 1 : Potential energy curve for an excimer molecule. R ~ rare gas atom, X ~ halogen atom, HX ~ halogen donor molecule. Scales are only approximate for KrF and XeF.

in nuclear pumped laser (NPL) simulation experiments. This accelerator provides a low energy, low intensity, pulsed proton beam for use in studying potential NPL systems. Given such an experimental situation, we may ask the following questions.

(1) Can basic parameters (e.g. rate constants or excited state lifetimes) be determined for the NPL system under study?

(2) Does energy input using the particle accelerator accurately simulate the environment in an NPL system (e.g. a system pumped by the ^{3}He (n,p)^{3}H reaction)?

(3) What can be said about absolute conversion efficiencies for a particular NPL system (i.e. with what efficiency is proton energy converted to photon energy)?

The information presented in the remainder of this report concerns these questions. Section II describes our experimental arrangement. Section III presents the results of basic parameter measurements, and Section IV contains the results of absolute intensity measurements. Conclusions and comments are presented in Section V.

II. EXPERIMENTAL ARRANGEMENT

A. Accelerator

Experiments have been performed using Auburn University's Dynamitron accelerator. This machine is equipped with an ORTEC Duoplasmatron Ion Source and an ORTEC Model 510 Nanosecond Pulsing System [9] and is capable of producing direct current or pulsed beams of hydrogen, deuterium, or helium ions at a maximum energy of 3.5 MeV. The following information is taken from reference [10] and describes parameters for the accelerator when it is operated in the pulsed mode.

Direct current beams are extracted from the ion source and swept just above an aperture by a sinusoidal voltage of variable amplitude and 2 MHz frequency. At appropriate times the beam is allowed to sweep across the aperture to produce a gaussian-shaped pulse of approximately 50 ns FWHM. The time between pulses is variable from 1 μs to 32 ms, and each pulse is then Klystron bunched to achieve a minimum pulse width of approximately 3 ns FWHM.

Beam pulse parameters are measured using three different methods.

(1) An ORTEC fast faraday dup is placed on a exit port of the beam analyzing magnet, and the cup is connected to a fast oscilloscope with a short (< 3 feet) piece of RG-8 cable. This cable is terminated in 50 ohms at the oscilloscope. Peak currents of 800 μA and pulse widths of 2.5 ns can be measured in this configuration.

(2) Some 30 feet further along the beam flight path, a LiF target is placed at the entrance to the scintillation cell (see Figure 3). Six MeV γ-rays from the $^{19}F(p, {}^{4}He\ \gamma)^{16}O$ reaction are detected

using a plastic scintillator mounted on an RCA 8575 photomultiplier tube. Fast timing signals from the tube and its associated electronics are used to start a time-to-amplitude converter (TAC). Stop signals for the TAC are delayed appropriately after being generated by a time pick off unit which senses the approach of each beam pulse to the target. Output signals from the TAC are observed with a multichannel analyzer. Gamma rays from the $^{19}F(p, {}^{4}He\ \gamma)^{16}O$ reaction are emitted during time intervals which may be considered instantaneous with respect to a nanosecond time scale. Any single event comprising part of the TAC spectrum can be associated with either a leading or trailing edge proton in the beam pulse. Therefore, the FWHM of the time peak in the TAC spectrum serves as a measure of the beam pulse width. Pulse widths of approximately 3 ns FWHM can be measured at the entrance to the scintillation cell using this method. Similar measurements show that this pulse width increases to approximately 7 ns just after the beam pulse passes through the entrance foil of the scintillation cell. This foil is a 0.1 mil Havar alloy.

(3) During actual data acquisition, the scintillation cell serves as a faraday cup, and the beam pulse is again monitored with RG-8 cable and a fast oscilloscope. FWHM values of approximately 6 ns are obtained, the observed difference being attributed to the fact the cell is not designed as a fast faraday cup. Proton straggling in the entrance foil also contributes to the increased pulse width.

B. Scintillation Cell and Gas Handling System

Gas mixtures flow continuously through the scintillation cell during data acquisition. This is accomplished by pumping on the output side of the cell with a small forepump. The gas handling system is shown in Figure 2. Three gases can be mixed with this system, and flow rates for the gases are monitored with mass flow meters and controlled with micrometer valves. The volume of the mixing cell is approximately 5 cc, and the total pressure in both the mixing cell and the scintillation cell is measured with an MKS Baratron pressure gauge.

The scintillation cell and the vacuum chamber in which the cell is housed are shown in Figure 3. The vacuum chamber is stainless steel and is equipped with a cold trap so that the scintillation cell and the internal detector mount can be cooled to liquid nitrogen temperatures. Thermal insulation for the cold trap is provided by the high vacuum ($\leq 5 \times 10^{-6}$ torr) between the trap and the body of the vacuum chamber. The scintillation cell is constructed from a 4 inch copper cube. The cell is electrically insulated from both gas feed lines and the support finger from the cold trap. The pulsed proton beam enters the cell through a 0.1 mil Havar foil which is attached to the cell as shown in Detail-A, Figure 3. Scintillations from the cell are viewed through CaF_2 windows (2 in O.D.) along a direction at right angles to the direction of the incident beam. These windows are attached as shown in Detail-B, Figure 3. Ordinary O-ring vacuum seals are not satisfactory at liquid nitrogen temperatures; however, the polyethylene seals work well when the gasket surfaces on the body of the cell are optically flat.[11] The spring washers keep uniform pressure on the windows and polyethylene gaskets while the cell cools.

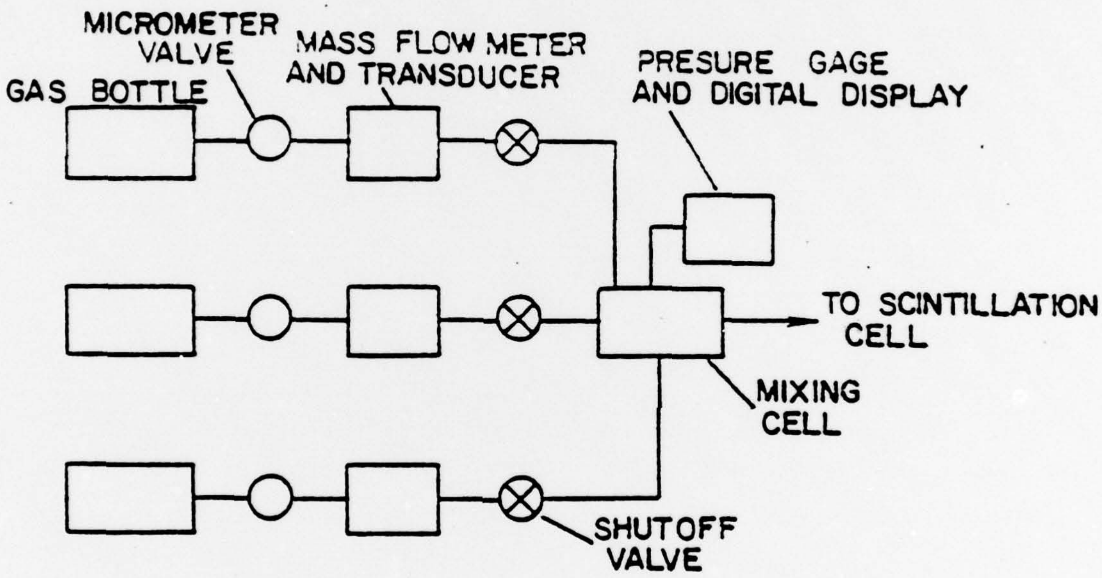

Figure 2 : Gas Handling System

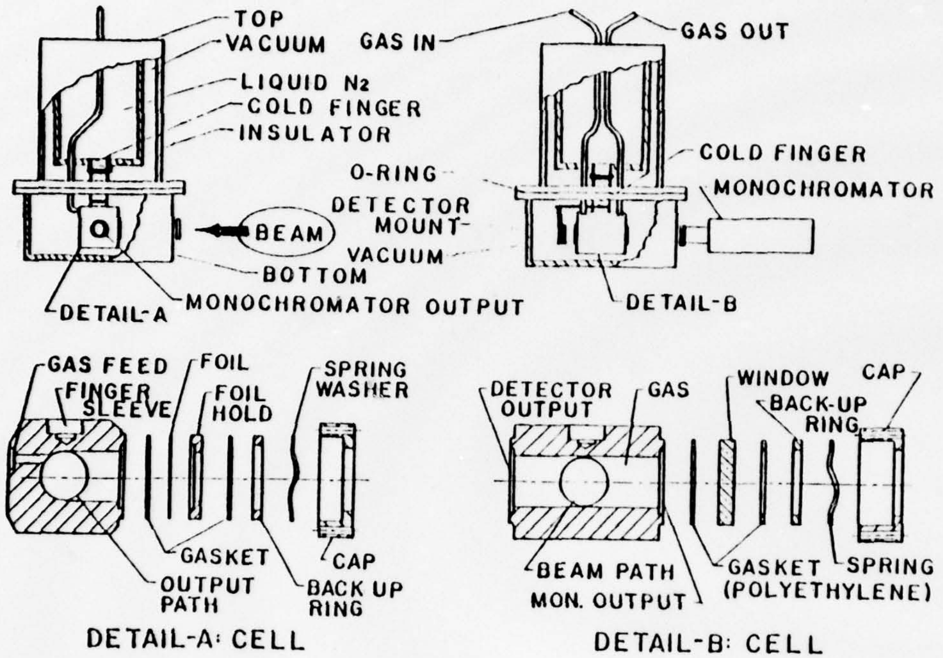

Figure 3 : Scintillation Cell

C. Data Acquisition System

A block diagram of the electronics used for data acquisition is shown in Figure 4. This system is similar to the single photon counting system employed by Hurst et. al.[12] Data are accumulated by counting single photons emitted from the scintillation cell. These scintillations are viewed with an RCA C31934 photomultiplier tube attached to a Jarrel-Ash 0.5 meter scanning monochromator. The system works in one of two modes.

(1) Lifetime Mode. Data acquired in this mode of operation are used to determine basic system parameters such as formation rate constants, excited state lifetimes, and quenching rate constants. For these measurements, the monochromator does not scan but rather is set to one wavelength of interest, and the system operates as follows. A fast timing signal is generated by the beam pick off system (BPO) as each beam pulse approaches the scintillation cell. This signal is delayed electronically in order to allow the beam pulse to enter the scintillation cell and excite molecular states of interest in the gas mixture. The probability for decay of one of these excited states is greatest immediately after its formation, and the probability decreases with passing time. The incident beam intensity is kept low so that approximately one photon is counted for every ten beam pulses. This photon will have been emitted at a time corresponding to some point on the decay curve associated with the excited state of interest. For each photon detected, a fast timing signal is generated and used to start a time-to-amplitude converter (TAC). The stop signal for the TAC is the fast timing signal from the beam pick off unit. This BPO signal is used

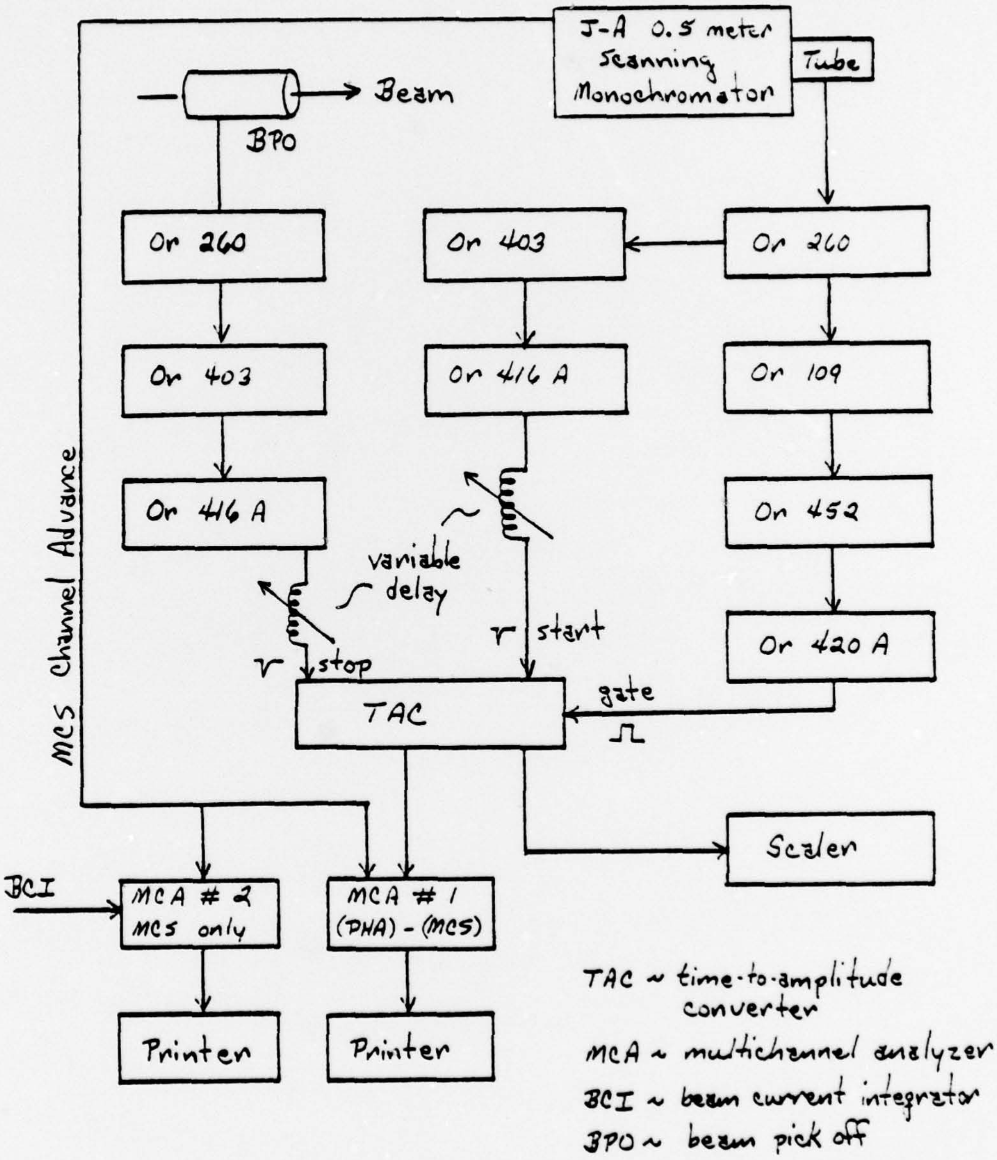

TAC ~ time-to-amplitude converter
MCA ~ multichannel analyzer
BCI ~ beam current integrator
BPO ~ beam pick off

Figure 4 : Electronics

as a time reference, and the TAC output is a voltage pulse whose amplitude is proportional to the time difference between the BPO signal and the fast timing signal from the photomultiplier tube. This voltage pulse is stored in multichannel analyzer number one (MCA #1) which operates in the pulse height analysis (PHA) mode. This process is repeated over a period of several minutes during which time many thousands of beam pulses enter the scintillation cell. The resulting TAC spectrum represents the decay in time of the excited state of interest. The TAC spectrum is gated with a slow logic signal generated using the linear signal from the phototube. This linear signal contains the energy information for any event detected in the phototube (see Figure 5). This procedure excludes from the TAC spectrum random events due to phototube noise and events resulting from multiple photon detection.

(2) Spectrum Mode. The data acquisition system operates in the spectrum mode for the absolute intensity measurements discussed in Section III. The drive motor for the grating in the monochromator runs at a constant speed, and the scan speed of the instrument (i.e. the speed at which the grating turns) is determined with a set of gears. The light chopper assembly shown in Figures 6 and 7 is attached to the shaft of the drive motor, and this system produces one square output pulse for each revolution of the shaft. These output pulses are spaced 5.23 seconds apart without reference to the speed at which the grating rotates. This output pulse is used to advance MCA #1 through successive channels when the analyzer operates in the multichannel scale (MCS) mode. While the analyzer sits in one channel for 5.23 seconds, the monochromator grating turns through some wavelength interval, and every photon detected in this interval produces a square, logic pulse which is stored in this one channel. This logic pulse is a second output signal from the TAC

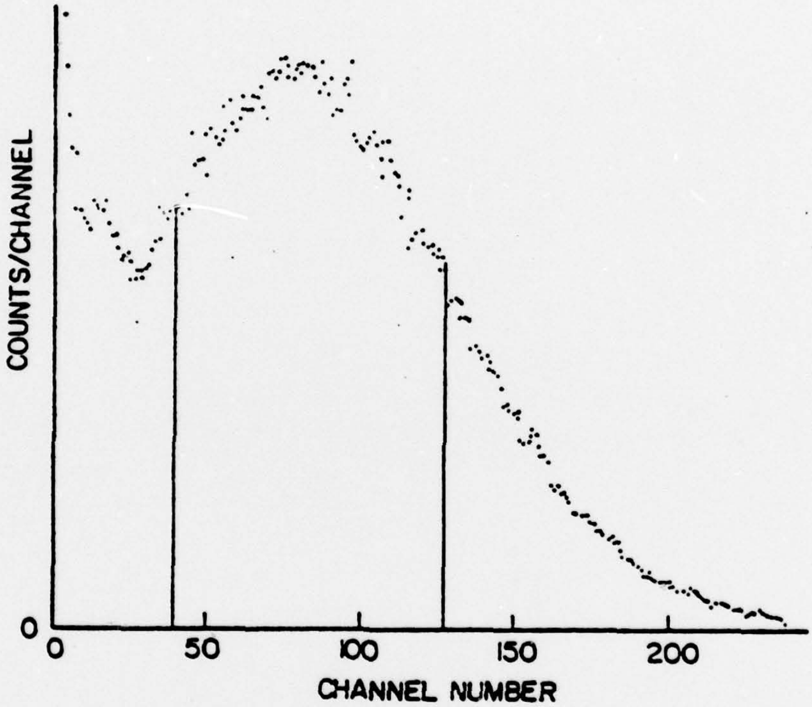

Figure 5 : Dynode (energy) signal spectrum from phototube. Vertical lines correspond to discriminator level settings.

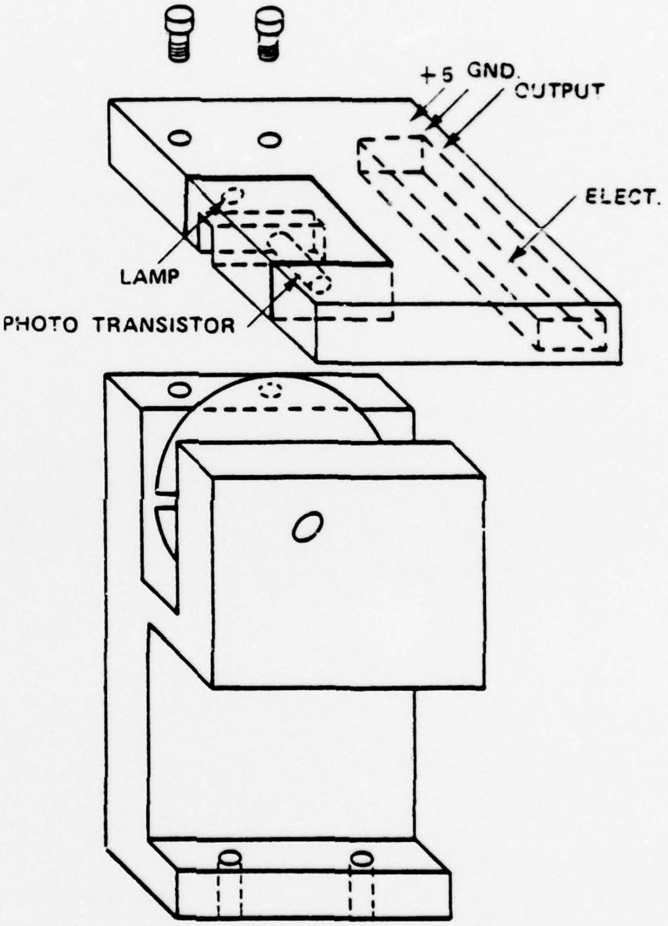

Figure 6: Monochromator Channel Advance
Light Chopper Assembly

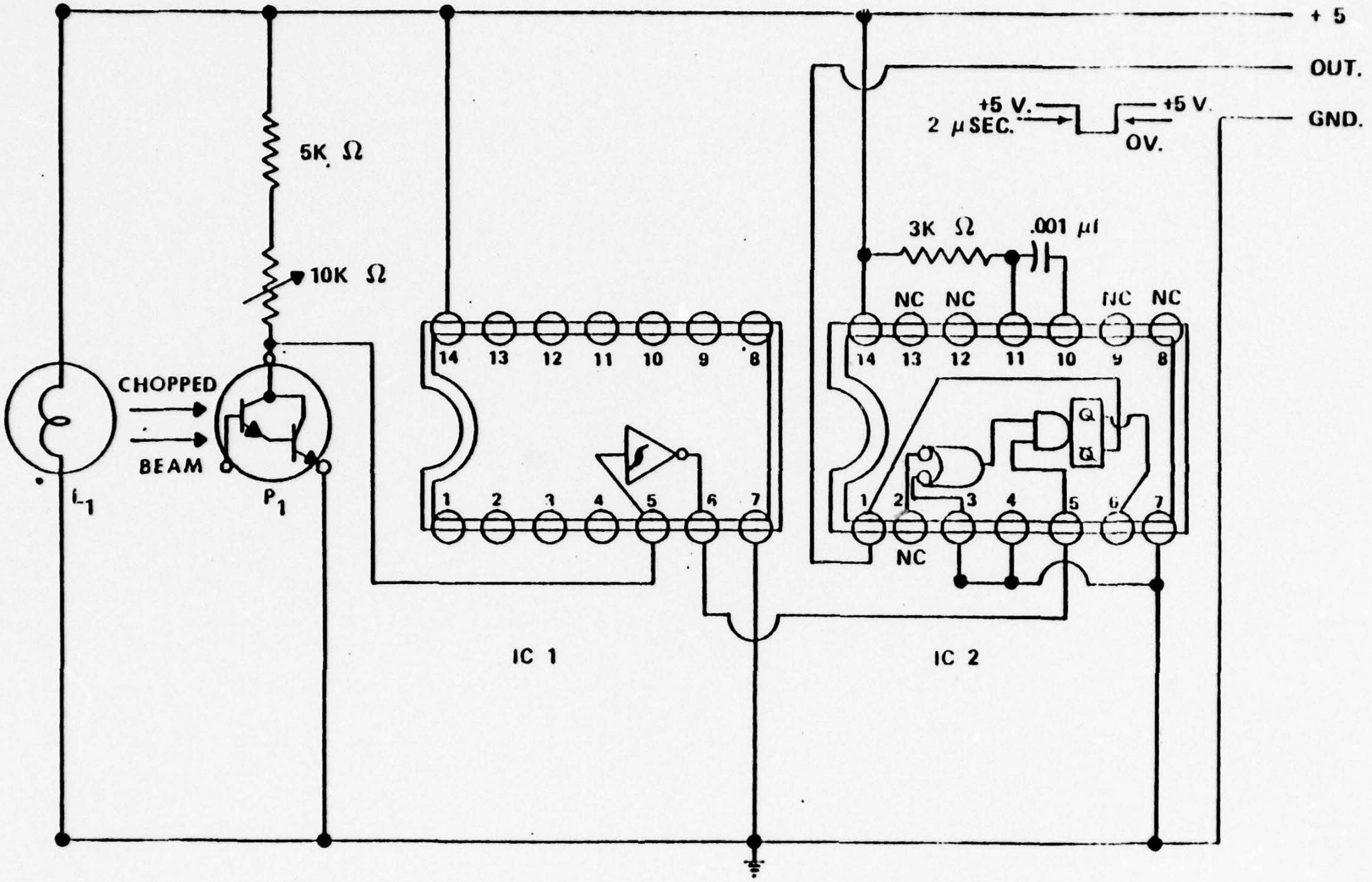

Figure 7 : Electronics for Monochromator Channel Advance. This electronics package is attached to the light chopper assembly as show in Figure 6.

which is generated each time the TAC produces a voltage pulse which would ordinarily be used when the system is in the lifetime mode. Thus a histogram of any feature of interest may be generated by having the monochromator scan through a particular wavelength interval (See Figure 8).

For both absolute and relative intensity measurements, the beam current incident on the scintillation cell must be accurately known. This is accomplished by using a second multichannel analyzer (MCA #2) which operates in the MCS mode. The channel advance signal for MCA #1 is also used to advance MCA #2 which counts the output signals from a beam current integrator. This procedure produces a second histogram which shows the behavior of the beam current as a function of time.

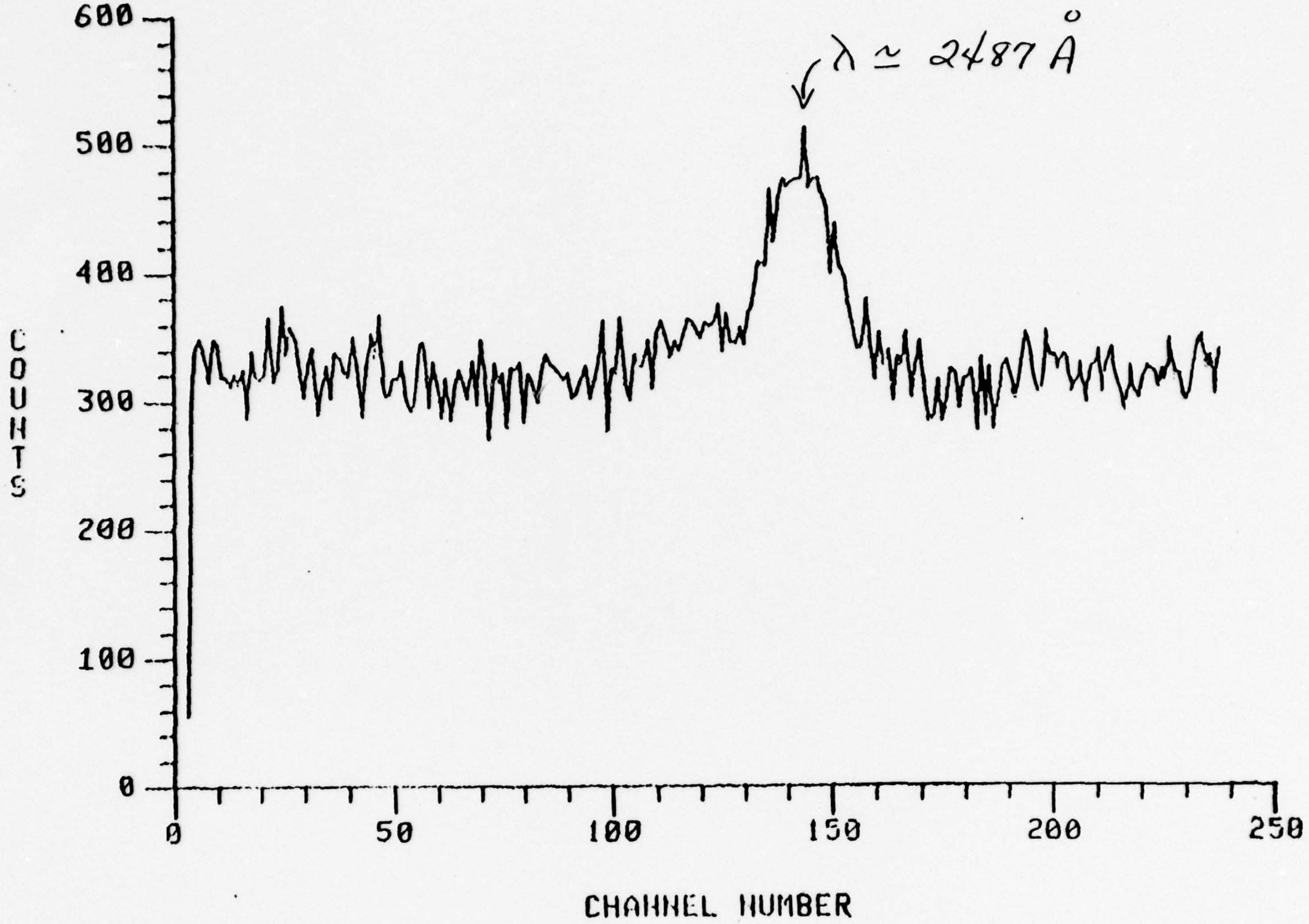

Figure 8 : Scan of KrF Feature

III. BASIC PARAMETER MEASUREMENTS

A. Theoretical Considerations

Our effort here at Auburn has been an experimental effort; however, we have enjoyed the benefits of having worked closely with Dr. Edward R. Fisher and his associates at Wayne State University, Detroit, MI. Dr. Fisher has developed a fully time dependent numerical model characterizing proton beam driven gas mixtures which are of interest as potential NPL systems.[13] We have studied low total pressure (< 50 torr) mixtures of Kr-NF_3 and Xe-NF_3 in an effort to obtain basic parameter information for these systems. For these low pressures and under conditions of low energy deposition, calculations performed at Wayne State suggest a simple kinetics scheme for both the Kr-NF_3 and the Xe-NF_3 systems. These calculations also indicate that the formation rate constant, K_1, for the reactions

$$Kr^*(^3P_2) + NF_3 \xrightarrow{K_1} KrF^* + NF_2 \qquad (1)$$

and

$$Xe^*(^3P_2) + NF_3 \xrightarrow{K_1} XeF^* + NF_2 \qquad (2)$$

should come directly from experimental measurement. These two equations describe the formation of KrF^* and XeF^* via the excited state channel where the $^3P_2$ state is the metastable state in both Kr and Xe. When energy is deposited in these low pressure gas mixtures by low intensity proton beams, the number of noble gas ions created exceeds the number of $^3P_2$ excited states. However the ion channels

$$Kr^+ + F^- \xrightarrow{\beta_1} KrF^* \qquad (3)$$

and

$$Xe^+ + F^- \xrightarrow{\beta_1} XeF^* \qquad (4)$$

do not dominate the excited state channels because the free electron density in the system remains low. This low electron density coupled with very low NF_3 partial pressures ($\simeq$ 0.1 torr) does not allow the formation of large numbers of F^- ions. Thus the excited state channel dominates the ion channel even though the formation rate constant for the ion channel is much larger than K_1. The ion channel becomes dominant for systems normally considered for NPL operation.[14] These systems involve large energy deposition and high total pressure.

Now let us discuss the system kinetics which may be developed by considering only the excited state channel in the formation of the rare gas halides, KrF and XeF. The following development applies to both systems. The KrF system is used as an example. We begin with the following set of equations.

$$\mathrm{Kr} + \mathrm{proton} \longrightarrow \mathrm{Kr}^* + \mathrm{proton} \qquad (5)$$

$$\mathrm{Kr}^* + \mathrm{NF}_3 \xrightarrow{K_1} \mathrm{KrF}^* + \mathrm{NF}_2,\ K_1 \text{ in cm}^3/\text{sec} \qquad (6)$$

$$\mathrm{KrF}^* \xrightarrow{K_2} \mathrm{Kr} + \mathrm{F} + h\nu,\ K_2 \text{ in sec}^{-1} \qquad (7)$$

$$\mathrm{KrF}^* + \mathrm{NF}_3 \xrightarrow{K_3} \mathrm{Kr} + \mathrm{F} + \mathrm{NF}_3,\ K_3 \text{ in cm}^3/\text{sec} \qquad (8)$$

$$(\mathrm{Kr}^*) = (\mathrm{Kr}^*)_o \text{ at } t = 0 \qquad (9)$$

K_1 is the formation rate constant, K_2 is the inverse of the natural radiative lifetime of KrF^*, and K_3 is the rate constant for the quenching of KrF^* by NF_3. The initial concentration of Kr^*, $(Kr^*)_o$, is assumed known at time t = 0 which is immediately after the beam pulse traverses the scintillation cell. Equations (6) through (8) lead to the following rate equations.

$$\frac{d}{dt}(Kr^*) = -K_1(Kr^*)(NF_3) \qquad (10)$$

$$\frac{d}{dt}(KrF^*) = K_1(Kr^*)(NF_3) - K_2(KrF^*)(NF_3) \qquad (11)$$

The parenthesis terms in equations (10 and (11) have units of cm^{-3}. Equations (9), (10), and (11) can be solved for the time dependence of the KrF^* concentration.

$$(KrF^*) = \frac{(Kr^*)_o}{1 - \frac{K_2 + K_3(NF_3)}{K_1(NF_3)}} \left[e^{-K_2 + K_3(NF_3)]t} - e^{-K_1(NF_3)t} \right] \qquad (12)$$

Equation (12) can be written in the following form which is more useful for comparison with experimental results.

$$\frac{d}{dt}\ln(KrF^*) = \frac{\overbrace{K_1(NF_3)e^{-K_1(NF_3)t}}^{1} - \overbrace{[K_2 + K_3(NF_3)]e^{-[K_2 + K_3(NF_3)]t}}^{2}}{\underbrace{e^{-[K_2 + K_3(NF_3)]t}}_{3} - \underbrace{e^{-K_1(NF_3)t}}_{4}} \qquad (13)$$

The left side of equation (13) is the destruction frequency for the KrF^* population. The dependence of this destruction frequency upon NF_3 Partial pressure can be determined directly by experimental measurement.

The formation rate constant, K_1, should be roughly the same order of magnitude as the total loss rate for Kr^* through all interactions. This total loss rate for Kr^* has been reported as 1.2×10^{-10} cm^3/sec.[8] The radiative lifetime of KrF^* and the quenching rate constant for KrF^* by F_2 have been reported as 6.5 nsec[4] and 7.8×10^{-10} cm^3/sec, respectively.[6] Order of magnitude values for the quantities $K_1(NF_3)$ and $K_2 + K_3(NF_3)$ may be calculated using these numbers and assuming an NF_3 partial pressure of one torr ($\approx 3.3 \times 10^{16}$ molecules/cm^3). These calculations show that $K_2 + K_3(NF_3)$ is an order of magnitude larger than $K_1(NF_3)$. Therefore, at long times into the decay of the KrF^* population, terms 2 and 3 in equation (13) may be neglected in comparison with terms 1 and 4. Equation (13) then reduces to

$$\nu \triangleq \frac{d}{dt} \ln(KrF^*) = K_1(NF_3) \qquad (14)$$

Thus the destruction frequency, ν, should depend linearly upon the NF_3 partial pressure, and slope of the resulting straight line should yield the formation rate constant, K_1.

B. Experimental Measurements

For the experimental results reported here, the data acquisition system was used in the lifetime mode (see section II C). The Dynamitron accelerator furnished gaussian-shaped pulses of 2MeV protons approximately 6 ns FWHM and 64 μs apart. The number of protons per pulse was kept low (usually $10^6 - 10^7$ protons per pulse) so that approximately one photon was detected by the photomultiplier tube for every ten beam pulses entering the scintillation cell. Experimental measurements were performed by bombarding Kr - NF_3 and Xe - NF_3 gas mixtures and counting photons emitted in the decay of KrF^* ($\lambda = 2487\mathring{A}$) and XeF^* ($\lambda = 3525\mathring{A}$). The Kr and Xe partial pressures were held at 40 torr, and the NF_3 partial pressure was varied from 0.04 to 0.25 torr. Typical results for Kr - NF_3 and Xe - NF_3 are shown in Figures 9 and 10, respectively. Such curves as these were produced for a series of NF_3 partial pressures, and, for each curve, a destruction frequency, ν, was determined as indicated in Figures 9 and 10. These destruction frequencies were then plotted as a function of NF_3 partial pressure to give the results shown in Figures 11 and 12. In accordance with equation (14), the slope

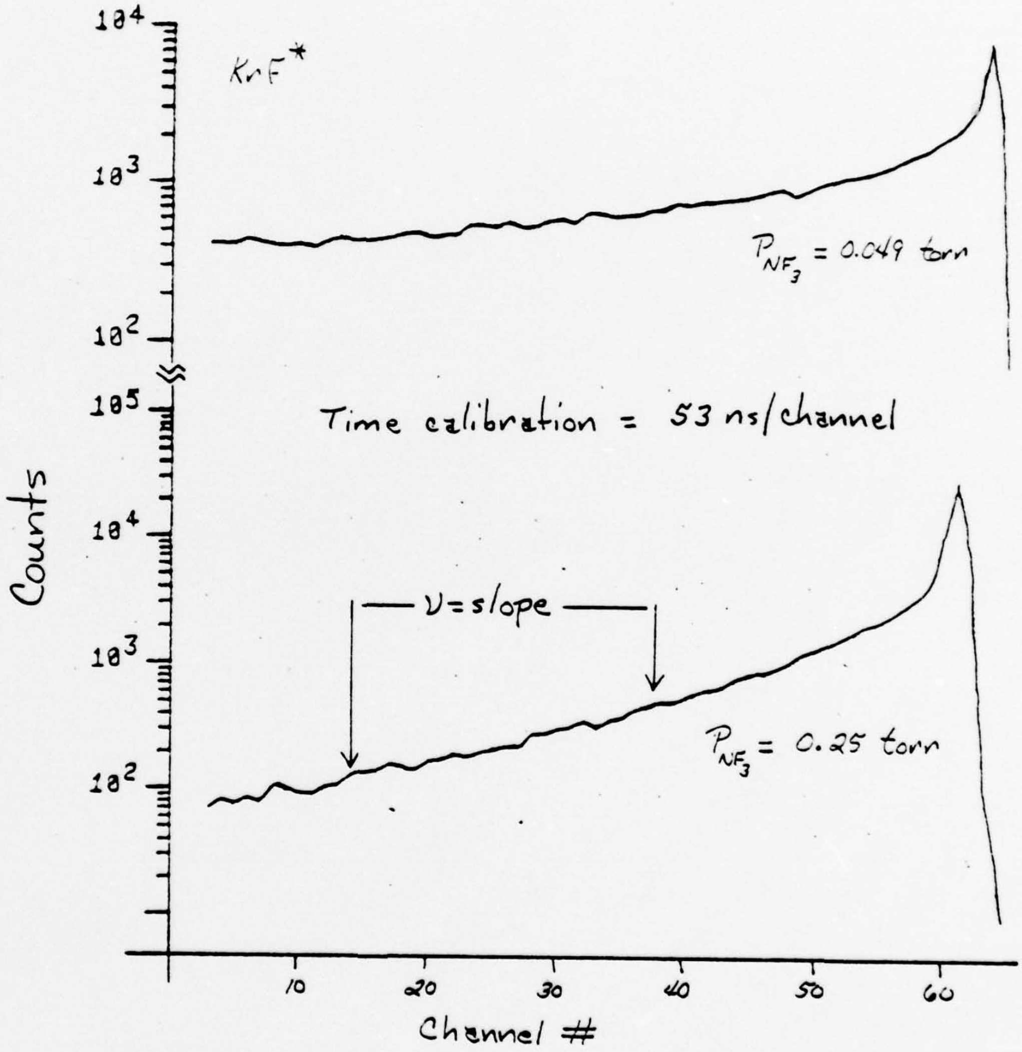

Figure 9 : Destruction Frequency Curves for P_{Kr} = 40 torr. ν = destruction frequency

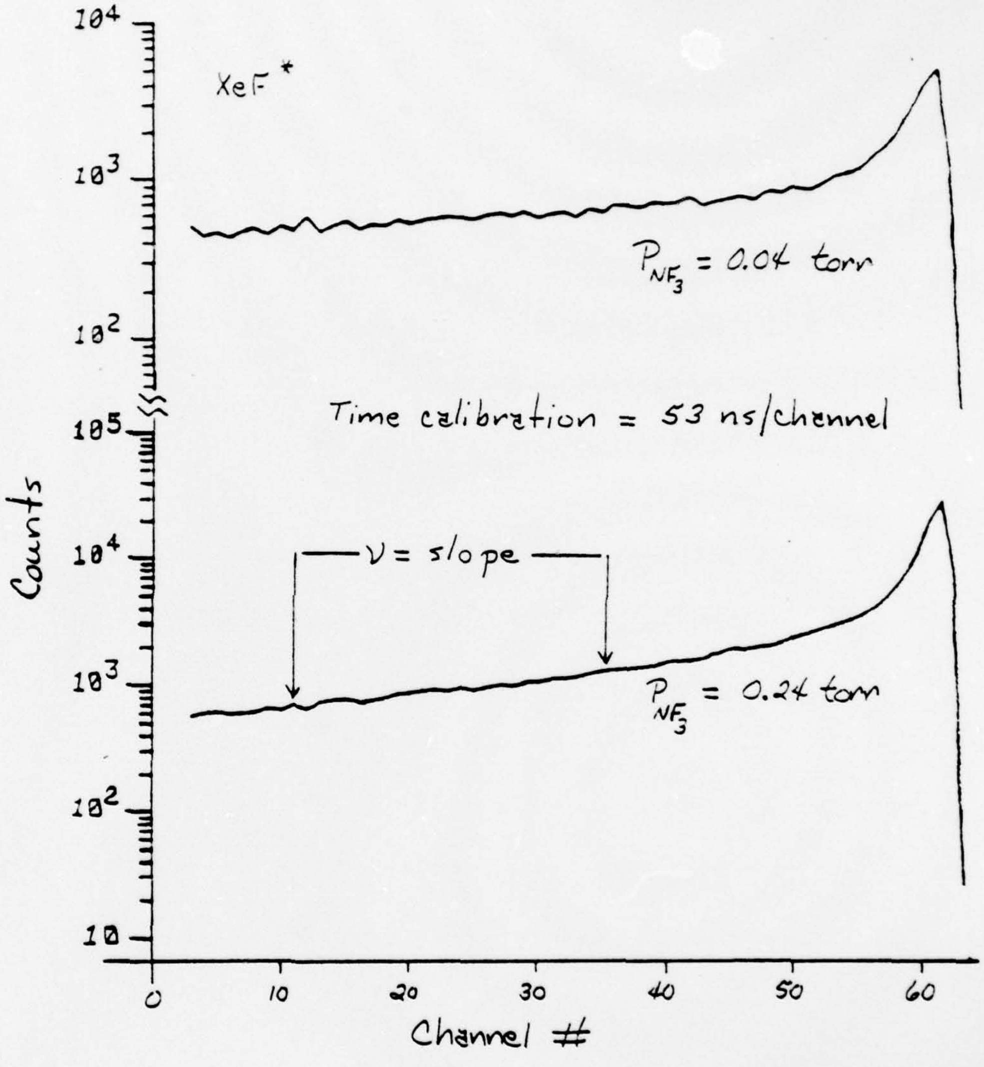

Figure 10 : Destruction Frequency Curves for P_{Xe} = 40 torr. ν = destruction frequency

Figure 11: Destruction Frequency, ν, Vs. P_{NF_3}

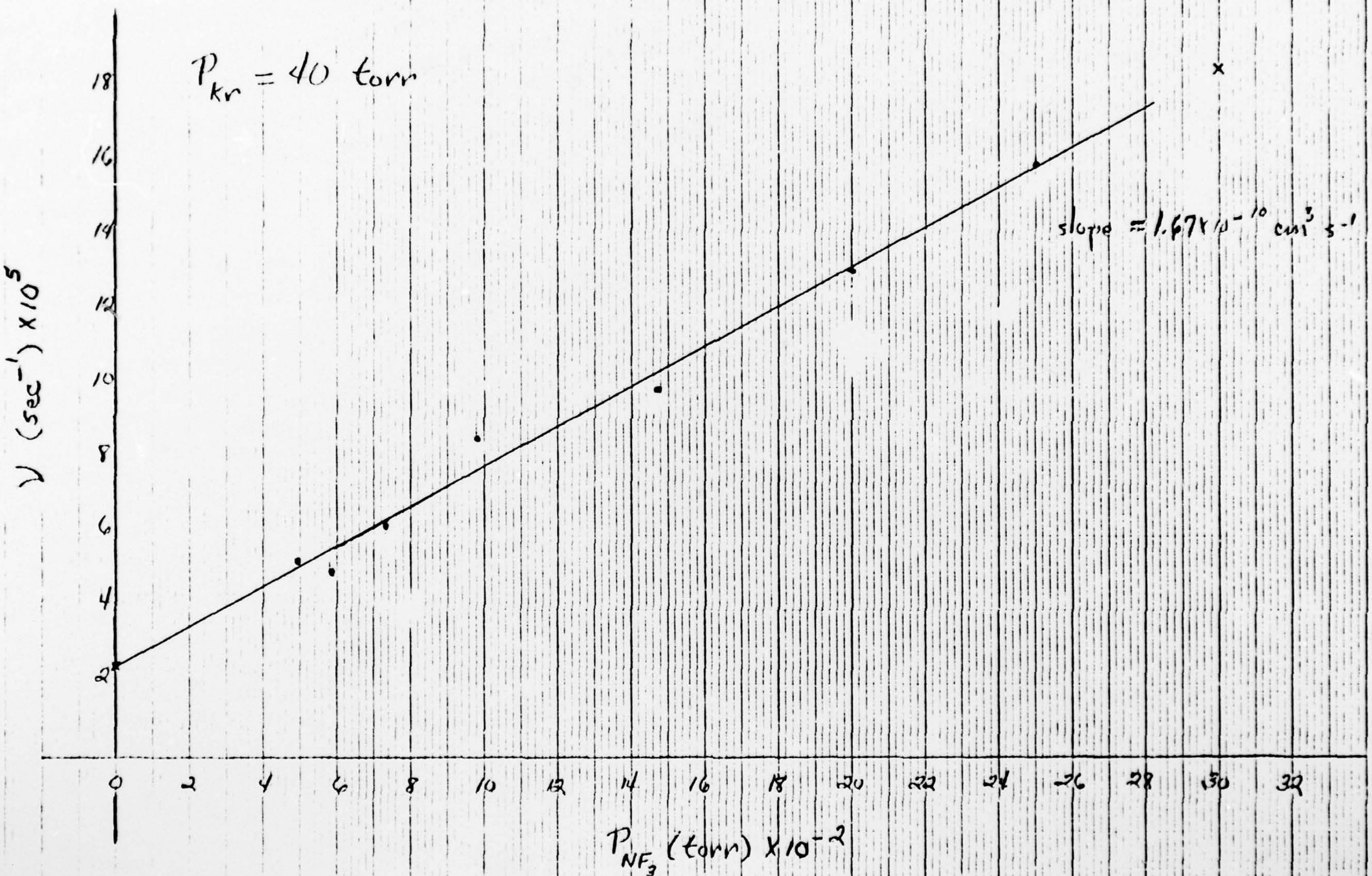

Figure 12: Destruction Frequency, ν, vs. P_{NF_3}

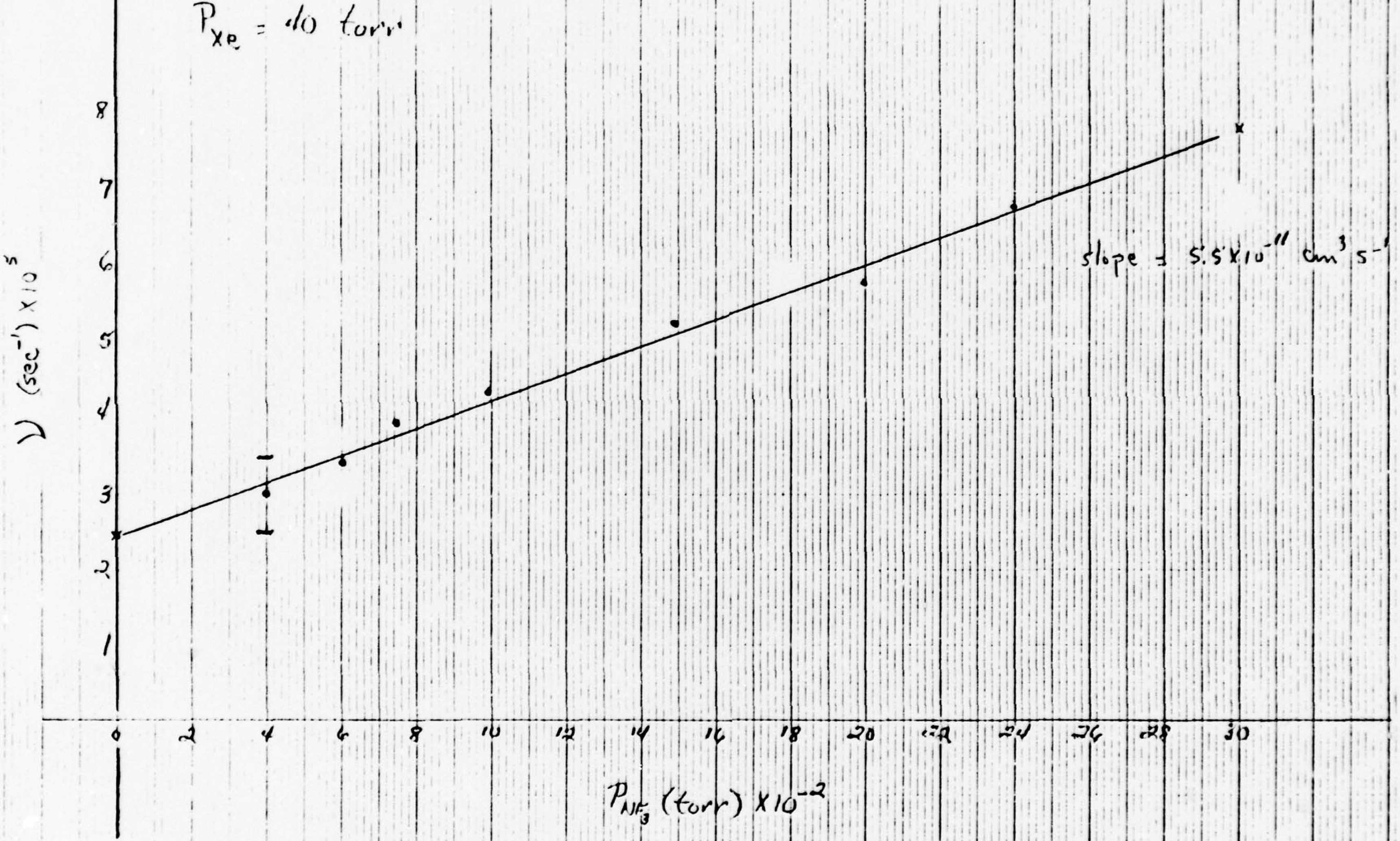

of the straight line in Figure 11 gives 1.7 x 10^{-10} cm^3/sec as the formation rate constant for the Kr - NF_3 system. The corresponding number for the Xe-NF_3 system is 5.5 x 10^{-11} cm^3/sec as determined from Figure 12. These numbers are believed accurate to within 25 percent.

Recall that the formation rate constants presented here represent the loss of Kr^* and Xe^* via the reactions

$$Kr^*(^3P_2) + NF_3 \xrightarrow{K_1} KrF^* + NF_2$$

and

$$Xe^*(^3P_2) + NF_3 \xrightarrow{K_1} XeF^* + NF_2.$$

In the following table, these rate constants are compared to total quenching rate constants taken from reference 8. These total rate constants represent the loss of Kr^* and Xe^* due to all processes in Kr - NF_3 and Xe - NF_3 mixtures.

Table 1

System	$K_1(cm^3/sec)^+$	$\sum K_{loss}(cm^3/sec)^*$
$Xe + NF_3$	5.5 x 10^{-11} ± 25%	9 x 10^{-11}
$Kr + NF_3$	1.7 x 10^{-10} ± 25%	1.2 x 10^{-10}

+ This study

* Reference 8

The results for the Kr - NF_3 system attract additional attention upon first consideration. However, these two numbers compare quite reasonably when experimental errors are considered.

Several other interesting points are noted when the results of the present measurements are compared with calculations performed at Wayne State. First, equation (14) indicates a zero intercept for a plot of destruction frequency versus NF_3 partial pressure. However, as shown in Figures 11 and 12, this zero intercept is not observed experimentally. One possible explanation for this situation is that terms 2 and 3 cannot be completely neglected in equation (13). Chen and Payne [15] have investigated Kr-F_2 mixtures using low intensity, pulsed proton beams, and their plot of KrF^* destruction frequency versus F_2 partial pressure does intercept zero. However, their measurements were made at approximately 600 torr total pressure where we feel that careful consideration must be given to the ion reaction channel.

Figures 9 and 10 show that the decay curves for KrF^* and XeF^* are each comprised of two components, one representing a fast decay and the other a slow decay from which we have extracted the formation rate constants for the excited state channels. This two component decay is also observed by Chen and Payne [15] for the Kr-F_2 system. Initial calculations at Wayne State involved only the $^3P_2$ metastable states in Kr and Xe, and these calculations indicated only one component decays for KrF^* and XeF^*. However, more recent calculations have produced the results shown in Figure 13 for the decay of KrF^*. In addition to the $^3P_2$ metastable state, these calculations include a second excited state in Kr (e.g. the Kr^* ($^1P_1$) state), and the results appear to be in better agreement with the experimental measurements, indicating that higher excited states in Kr with large rate constants possibly play an important role in the formation and decay of KrF^*. [13]

Next, consider the time scales for Figures 9 and 10. Fluorescence is observed experimentally over a much longer time interval than is indicated in Figure 13. For example, the rise time for the fluorescence signal in Figure 9 is approximately 250 ns while the calculated value from Figure 13 is only 25 ns. No satisfactory explanation for this discrepancy exists at the present time.

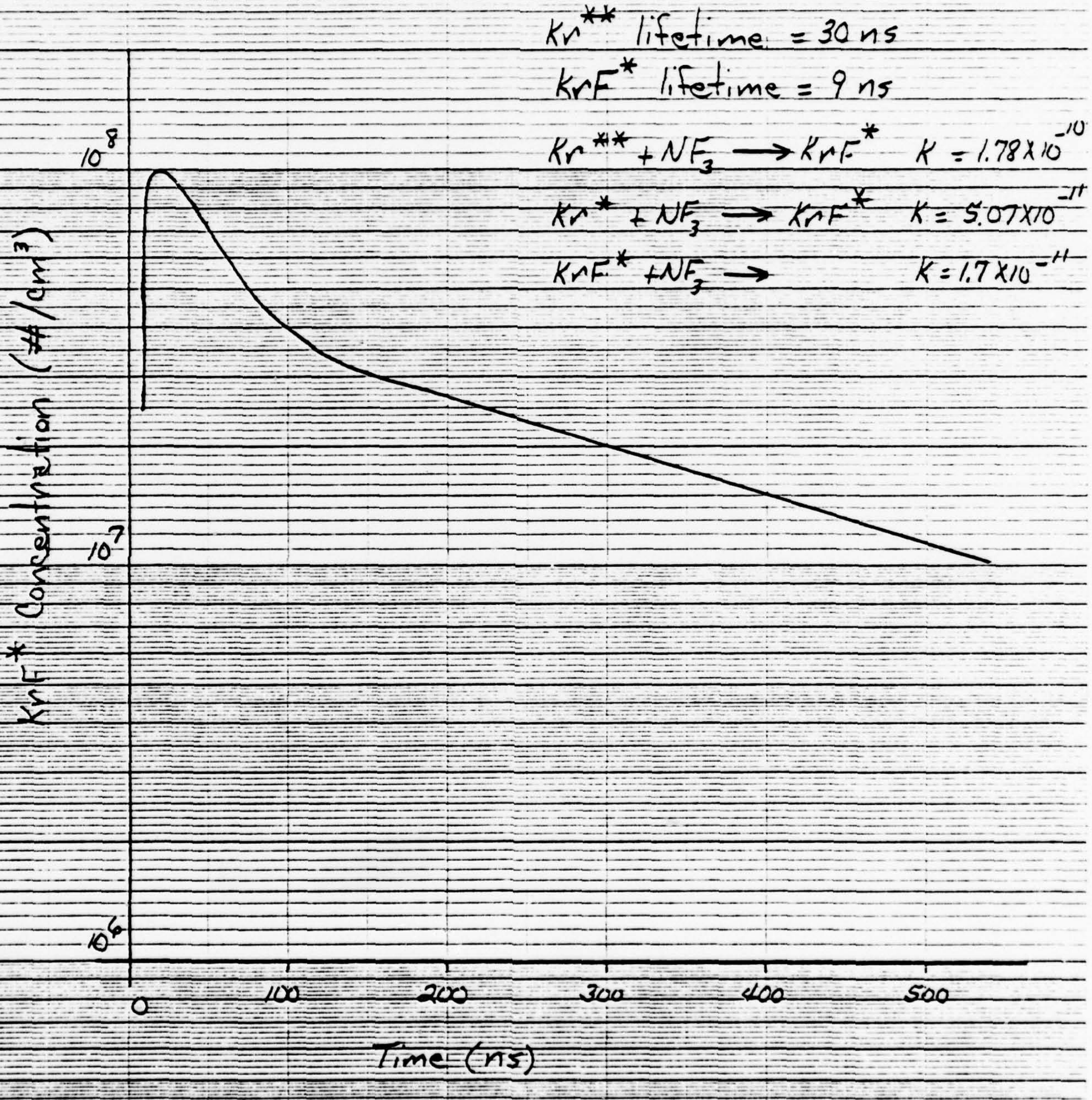

Kr^{**} lifetime = 30 ns

KrF^* lifetime = 9 ns

$Kr^{**} + NF_3 \longrightarrow KrF^*$ $K = 1.78 \times 10^{-10}$

$Kr^* + NF_3 \longrightarrow KrF^*$ $K = 5.07 \times 10^{-11}$

$KrF^* + NF_3 \longrightarrow$ $K = 1.7 \times 10^{-11}$

Figure 13: KrF^* Number Density. This Figure is reproduced from reference 13. Two excited state in Kr are included in this calculation.

Destruction frequency measurements similar to those discussed above were also attempted for Kr and Xe partial pressures of 200 torr and NF_3 partial pressures ranging from 0.2 to 1.0 torr. In all of our measurements, we mixed pure NF_3 with pure Xe or Kr, and, for large Xe and Kr partial pressures, this mixing procedure required that we use higher NF_3 partial pressures ($\simeq$ 1.0 torr for P_{Kr} = 200 torr compared with $\simeq$ 0.2 torr for P_{Kr} = 40 torr). The photocathode in our phototube is sensitive to γ-radiation, and, at higher NF_3 partial pressures, 6 MeV γ-rays from the $^{19}F(p, \alpha\ \gamma)^{16}O$ reaction could be observed. These γ-rays added to the noise contribution from the phototube. The decay frequency spectra were corrected for this noise contribution by covering the monochromator slits and subtracting noise counts from a particular spectrum for similar conditions of time, gas pressure, and beam current. However, even with these corrections, the data at 200 torr were inconsistent, and none of the results are included in this report. We feel that one possible explanation for the observed inconsistency is increased competition between the ion channel and the excited state channel at higher pressure.

IV. ABSOLUTE INTENSITY MEASUREMENTS

The information presented in this section concerns the efficiency with which the energy in the incident proton beam is converted to photon energy for the systems Kr-NF_3-UF_6 (λ = 2487 Å) and Xe-NF_3-UF_6 (λ = 3525 Å). The addition of UF_6 to any of the noble gas systems is desireable since the UF_6 could possibly supply both the fissionable material, ^{235}U, and the halogen atom required for the formation of the noble gas excimer Conceptually, these considerations point to a gaseous core reactor-laser systems supplying large amounts of power in the form of laser output.

Conversion efficiencies were determined by first performing relative intensity measurements. A method was then devised whereby these relative measurements were converted to give absolute results.

A. Relative Intensity Measurements

Relative intensity measurements were performed with the data acquisition system in the spectrum mode (see Section II C). Typical time averaged beam currents ranged from 100 to 200 namps with a pulse repetition rate of 16 μs. Initial interest was in mixing small amounts of UF_6 with low pressure ($\approx$ 40 torr) Kr and Xe. These measurements were performed at low pressure because the vapor pressure of UF_6 is approximately 50 torr at room temperature. Thus the UF_6 does not flow when the partial pressures of other gases in the system exceed 50 torr by any substantial amount.

No fluorescence was observed from the Kr and Xe systems with only UF_6 added. Therefore, a small amount of NF_3 was added to each system and held constant while the UF_6 partial pressure was varied. The appropriate NF_3 partial pressure was determined from the relative intensity curves shown in Figure 14. Kr and Xe partial pressures were

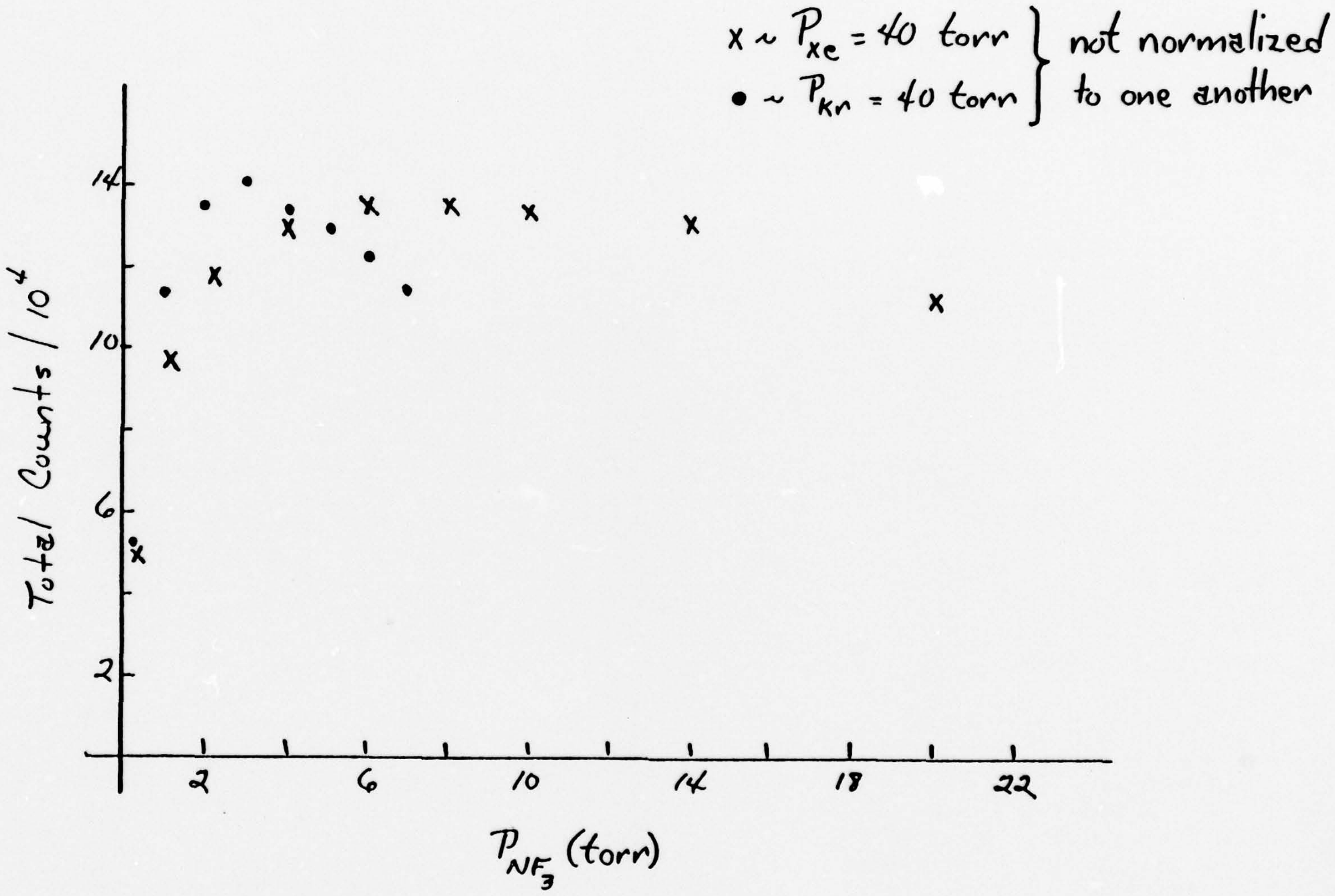

Figure 14 : XeF and KrF Relative Intensity Curves

held constant at 40 torr, and the NF_3 partial pressure was varied from 0 to 20 torr. Each point on the curves in Figure 14 was computed using a scan of the feature of interest such as shown in Figure 8. Each of these scans was integrated, corrected for background, and normalized to a constant amount of beam current. No other features of the data acquisition system (e.g. discriminator levels, monochromator slit widths, etc.) were changed during data acquisition. NF_3 partial pressures of two torr and four torr were selected for the Kr and Xe systems, respectively.

The results of adding UF_6 to low pressure Kr-NF_3 and Xe-NF_3 mixtures are shown in Figure 15. Similar curves comparing results for low and high pressure Xe systems are shown in Figure 16. The data points on the curve for a Xe partial pressure of 300 torr were taken statically (i.e. without gas flow through the scintillation cell). The cell was filled to 300 torr of Xe, 30 torr of NF_3, and a given UF_6 pressure. Data were taken for approximately 15 minutes after which the cell was pumped out, refilled, and the process repeated for a different UF_6 pressure. Results from this type of measurement are considered less accurate than those made with gas flow through the cell, primarily because the UF_6 tends to settle out and coat the cell walls during the static measurements.

Figures 15 and 16 show that the fluorescence from both the Kr and Xe systems is sharply reduced by the addition of small amounts of UF_6. The optical absorption cross section, σ, for UF_6 as a function of wavelength is shown in Figure 17.[3] For KrF^*, $\sigma \simeq 2 \times 10^{-18}$ cm^2, and for XeF^*, $\sigma \simeq 6 \times 10^{-21}$ cm^2. Photons travel an average distance of about 5 cm in order to escape the scintillation cell used for these measurements. Assuming an initial flux, ϕ_o, of photons, the decrease

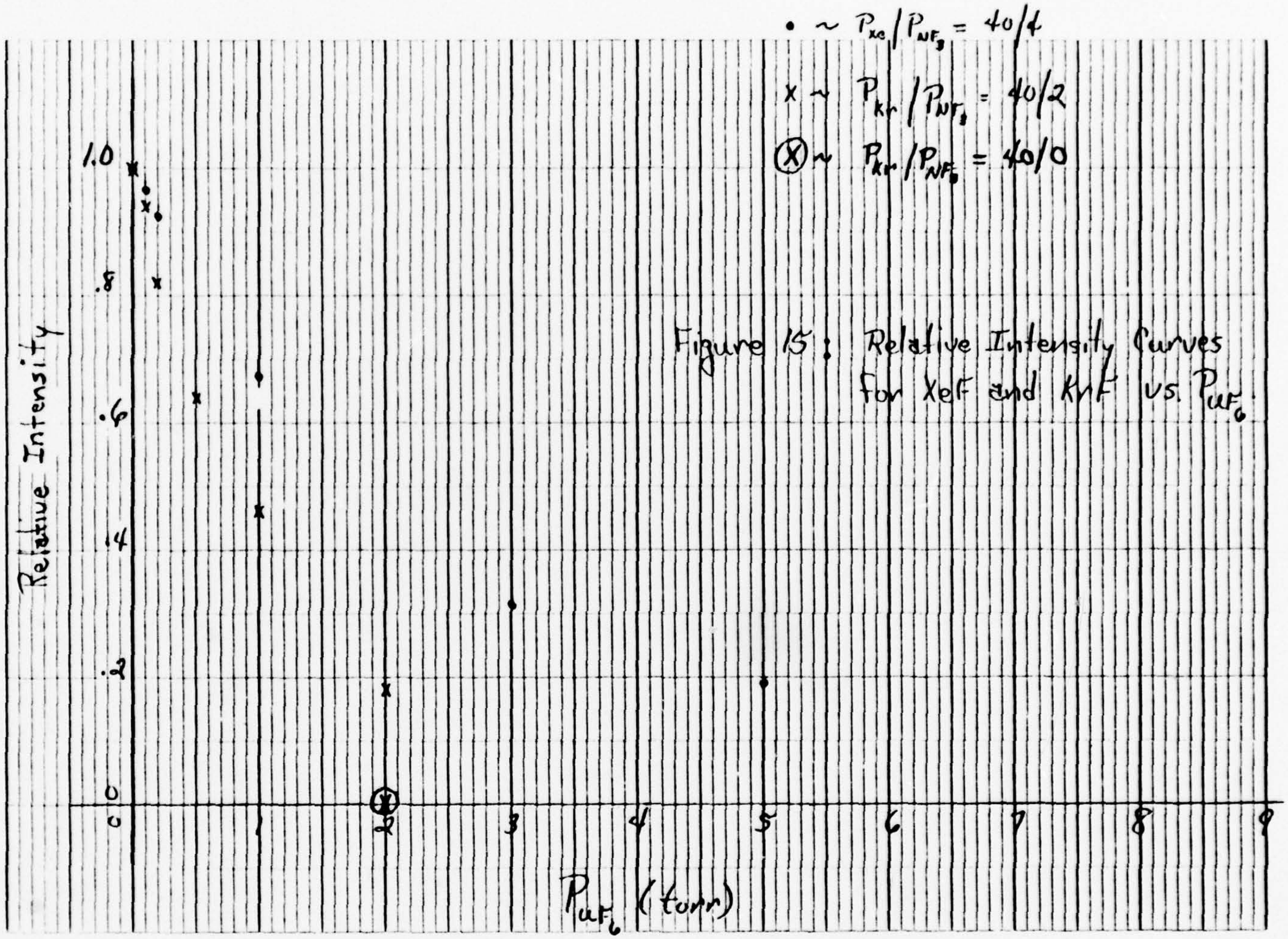

Figure 15: Relative Intensity Curves for XeF and KrF vs. P_{UF_6}

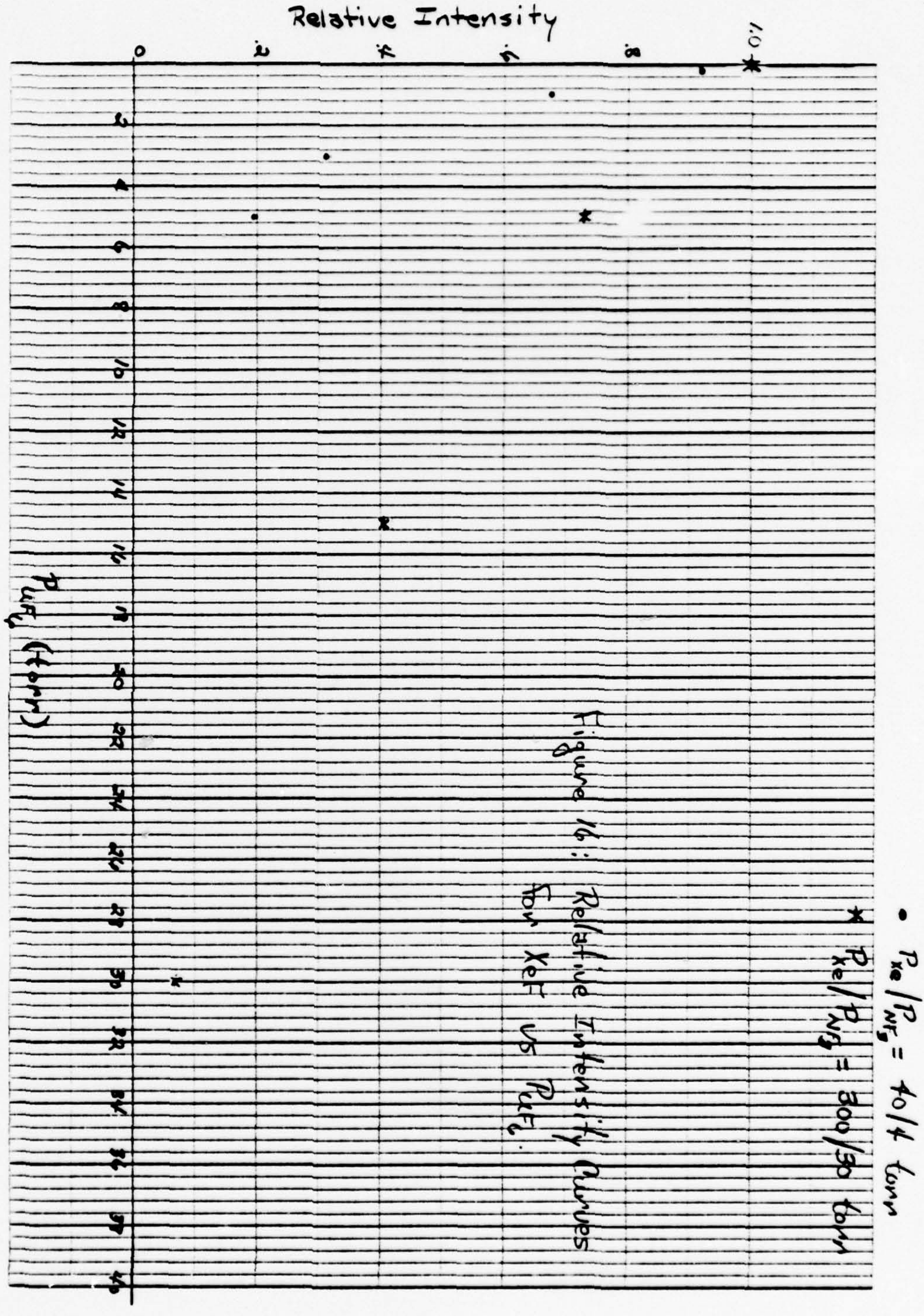

Figure 16: Relative Intensity Curves for XeF vs P_{NF_3}.

Figure 17: Optical Absorption Cross Section for UF_6

Data by De Poorter and Rofer - De Poorter
Taken from NPL's, G.H. Miley, Army Contract
#DASG60-77-C-0130

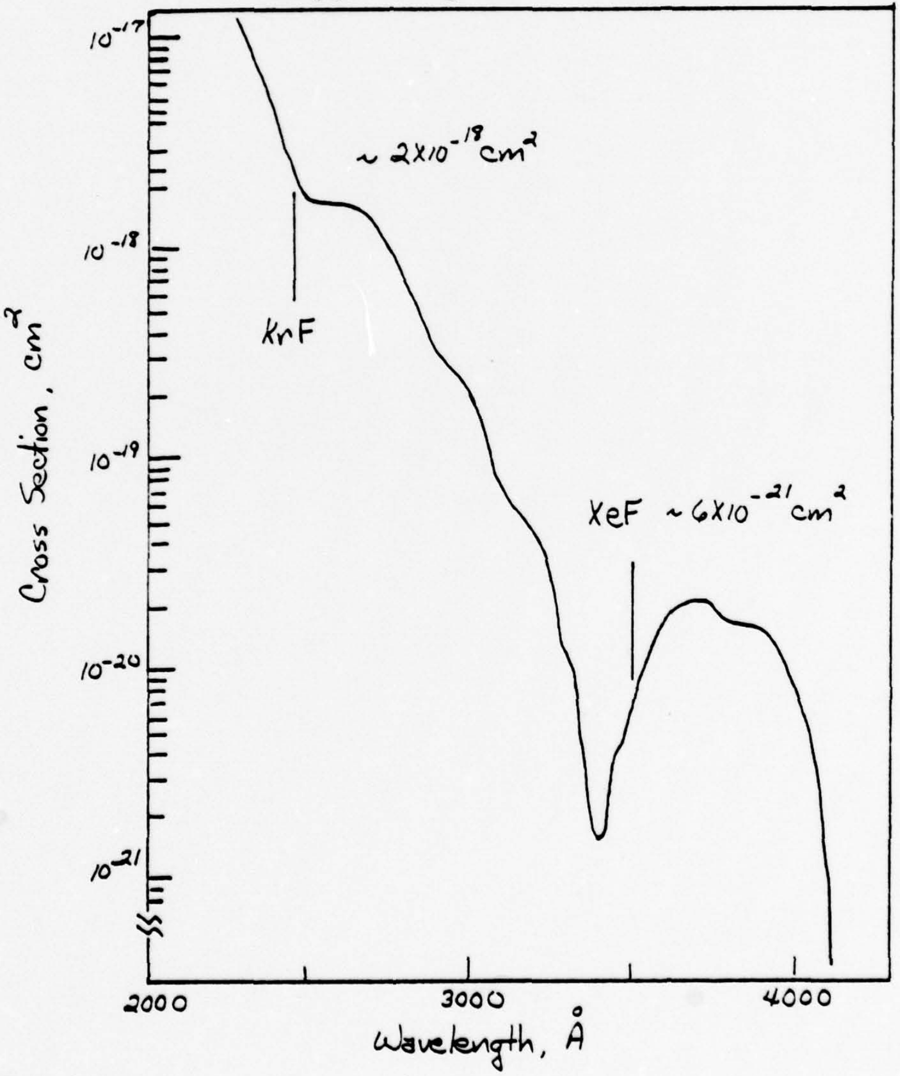

in the number of photons, $d\phi$, due to absorption over a path length, dx, can be written as

$$d\phi = -\phi n\sigma dx \qquad (15)$$

where n is the number density of UF_6 molecules. Simple integration gives

$$\phi/\phi_o = e^{-n\sigma x}, \quad x \simeq 5 \text{ cm} \qquad (16)$$

This equation can be used to construct the following table.

Table 2

P_{UF_6} (torr)	$n(\#/cm^3)$	$(\phi/\phi_o)_{KrF}$	$(\phi/\phi_o)_{XeF}$
0.25	8.13×10^{15}	0.9219	0.9998
0.50	1.63×10^{16}	0.8496	0.9995
1.0	3.25×10^{16}	0.7225	0.9990
2.0	6.51×10^{16}	0.5215	0.9980
3.0	9.76×10^{16}	0.3768	0.9971
5.0	1.63×10^{17}	0.1959	0.9951
15.0	4.89×10^{17}	0.0075	0.9854
30.0	9.78×10^{17}	0.0001	0.9710

These calculations indicate that our scintillation system should be optically "thick" for KrF flourescence but optically "thin" for XeF flourescence. However, these results are not supported by our expermental results shown in Figure 15. The sharply reduced XeF fluorescence is most likely due to strong collisional quenching by UF_6. This quenching is probably present in the KrF system also, along with strong optical absorption. Future work is now being planned to determine basic parameters for the $Xe-NF_3-UF_6$ system. Basic parameter measurements for this system are complicated by the fact that NF_3 must be added to produce fluorescence.

B. Absolute Intensity Measurements

The following discussion outlines the development of the method used to obtain absolute conversion efficiencies from the relative intensity curves shown in Figures 14, 15, and 16. This method consisted of having the monochromator and its associated electronics view emission from the gas cell and from a calibrated, tungsten filament lamp. All distances, slit widths, discriminator settings, etc. were carefully maintained during these measurements, and the total energy deposited in the gas by the proton beam was computed as described in reference 16. The efficiency of conversion from proton energy to photon energy was determined, and this result was used to determine the conversion efficiency for one point on each of the curves in Figures 14, 15, and 16. The remaining points on a particular curve were then normalized so that the absolute conversion efficiency could be obtained as a function of NF_3 or UF_6 partial pressure. It should be pointed out that during the normalization process, proton energy loss calculations were performed for each data point shown on a particular relative intensity curve.

The tungsten lamp was calibrated in a U. S. Army laboratory on the Redstone Arsenal, Huntsville, AL. The emissivity, $E(\lambda)$, was measured at 50 cm from the surface of the filament and given in joules/cm^2/sec/Å. This situation is different from most other standard lamps which have their emissivities quoted at their filament surfaces. A diagram of the calibration equipment is shown in Figure 18. The monochromator looks through the scintillation cell to see the lamp filament which is accurately located 50 cm away. All sapphire and CaF_2 windows used with the scintillation cell were kept in position during the scans of the tungsten lamp in order to keep reflection and absorption effects the same for both situations.

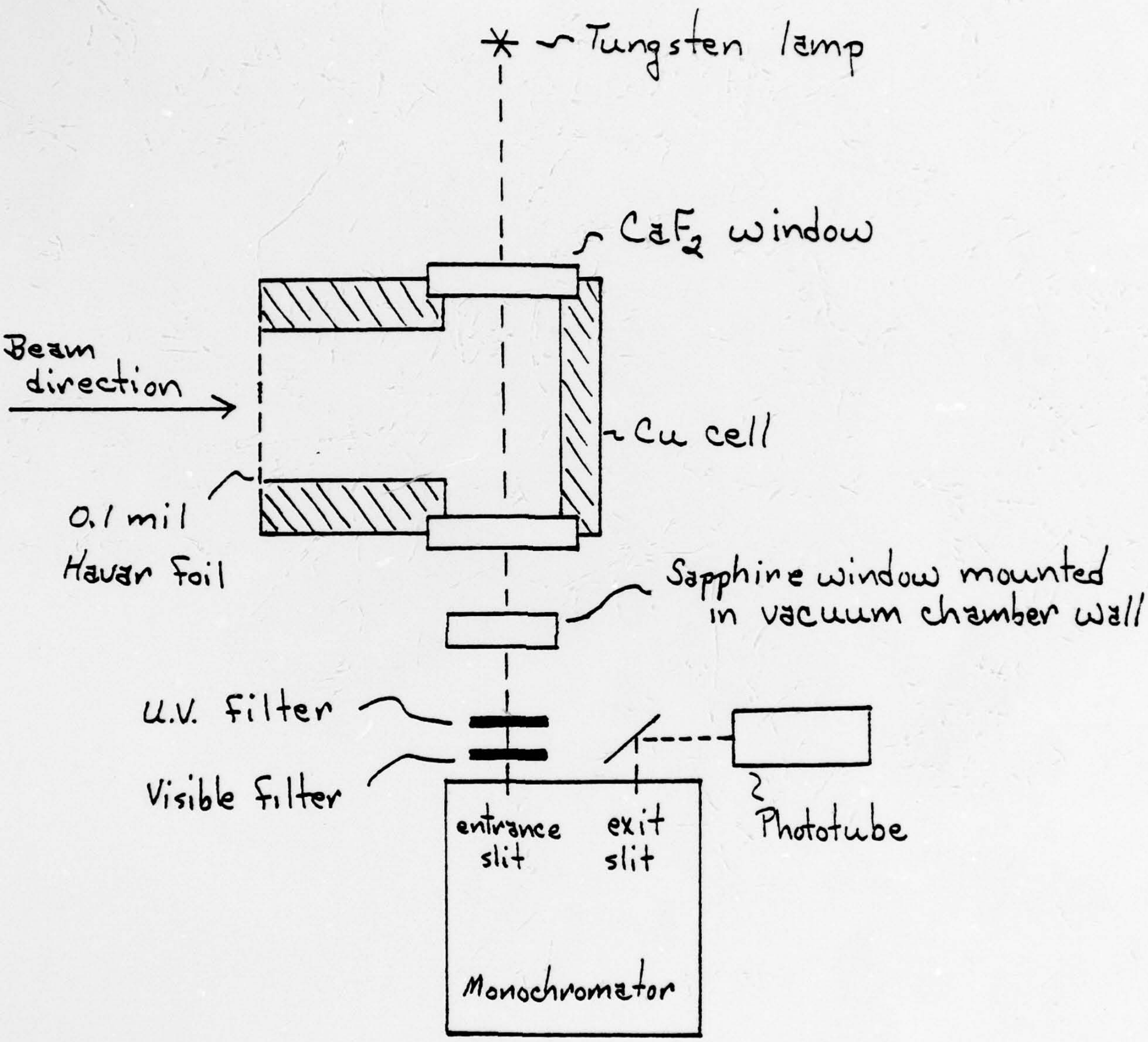

Figure 18 : Arrangement for Absolute Calibration Measurements. The tungsten lamp is accurately located 50 cm from the monochromator entrance slits.

The signal seen by the monochromator during a scan of the tungsten lamp may be written as follows.[17]

$$S_n'(\bar{\lambda}_n) = \int_{t_1}^{t_2} \int_{\lambda-\beta}^{\lambda+\beta} [E(\lambda')A_s]\, K(\lambda')\, d\lambda'\, dt \qquad (17)$$

$S_n'(\bar{\lambda}_n)$ is the signal strength in channel, n, of the multichannel analyzer. This signal is accumulated while the monochromator grating rotates for 5.23 seconds through some wavelength interval determined by the scan speed setting. Therefore we can write equation (17) as

$$S_n'(\bar{\lambda}_n) = T \int_{\lambda-\beta}^{\lambda+\beta} [E(\lambda')\, A_s]\, K(\lambda')\, d\lambda' \qquad (18)$$

where T = 5.23 seconds. $\bar{\lambda}_n$ is the average wavelength for the wavelength interval associated with channel, n. β is the ratio of the monochromator slit width, d, to the dispersion, D, of the monochromator. $E(\lambda')$ is the emissivity of the tungsten lamp at the wavelength λ', and A_s is the slit area. Recall for our situation that $E(\lambda')$ is evaluated at 50 cm from the filament of the lamp rather than at its surface. This results in the simple product, $E(\lambda')\, A_s$, for our situation rather than the more complicated expression given by Thomas in reference 17. Finally, $K(\lambda')$ is a measure of the detection sensitivity of the system as a function of wavelength.

Continuing according to Thomas, the emissivity, $E(\lambda')$, may be considered constant over the small wavelength interval $\lambda-\beta$ to $\lambda+\beta$. Therefore $E(\lambda')\, A_s = E(\bar{\lambda}_n)\, A_s$ and the product is taken outside the integral in equation (18). Evaluation of the remaining integral gives

$$S_n'(\bar{\lambda}_n) = T\, E(\bar{\lambda}_n)\, A_s\, K(\bar{\lambda}_n)\beta. \qquad (19)$$

In equation (19), the product $E(\bar{\lambda}_n)\, A_s\, \beta$ has units of photons per second. When this product is multiplied by T, the result is the total number of photons counted for one channel in our multichannel analyzer. $K(\bar{\lambda}_n)$ is a dimensionless quantity which represents the efficiency of the system.

During proton bombardment of a gas mixture, the monochromator looks at a cylindrical source whose length has been determined from geometrical considerations to be 2.63 cm. The diameter of the source is similar to the diameter of the proton beam which is approximately 0.5 cm. The signal from this line source seen by the monochromator may be written as

$$S_n(\bar{\lambda}_n) = \int_{t_1}^{t_2} \int_r \int_\Theta \int_\phi \frac{A_s \cos\Theta \cos\phi}{R^2} \cdot \frac{r^2 \sin\Theta\, dr\, d\Theta\, d\phi}{4\pi V} \cdot \int_{\lambda-\beta}^{\lambda+\beta} f(\lambda')K(\lambda')\,d\lambda'\,dt \qquad (20)$$

where R is the distance from the center of the line source to the center of the monochromator slits. V is the volume of the line source, and, for the line source, $f(\lambda')$ is the equivalent of the emissivity, $E(\lambda')$, for the tungsten lamp. The dimensions of the line source and the area of the monochromator slits are small compared to R so that the volume integral for the solid angle in equation (20) reduces to $A_s/4\pi R^2$. Making this substitution and then proceeding as with equation (18), equation (20) may be written as

$$S_n(\bar{\lambda}_n) = \frac{T\, A_s}{4\pi R^2}\, f(\bar{\lambda}_n)\, K(\bar{\lambda}_n)\, \beta. \qquad (21)$$

Combining equations (19 and (21)

$$f(\bar{\lambda}_n) = 4\pi R^2 E(\bar{\lambda}_n)\, \frac{S_n(\bar{\lambda}_n)}{S'_n(\bar{\lambda}_n)}. \qquad (22)$$

Recall that while the multichannel analyzer sits in channel, n, the monochromator grating scans through a wavelength interval, $\Delta\lambda$. Therefore, $f(\bar{\lambda}_n)\ \Delta\lambda$ is the number of photons of average wavelength, $\bar{\lambda}_n$, emitted per second from the 2.63 cm length of the line source.[18] When this product is summed over the total number of channels in a feature of interest, the result is

$$J_{kj} = 4\pi R^2 \Delta\lambda \sum_{i=1}^{n} E(\bar{\lambda}_i) \frac{S_i(\bar{\lambda}_i)}{S_i'(\bar{\lambda}_i)} \tag{23}$$

where R is the distance from the center of the line source to the center of the monochromator slits, and $\Delta\lambda$ is the wavelength interval through which the grating rotates in 5.23 seconds. $E(\bar{\lambda}_i)$ is the emissivity of the tungsten lamp at the wavelength $\bar{\lambda}_i$ which is the center wavelength in the wavelength interval associated with channel, i, of the multichannel analyzer. $S_i(\bar{\lambda}_i)$ is the signal from the scintillation cell, $S_i'(\bar{\lambda}_i)$ is the signal from the tungsten lamp, and n is the number of channels in the feature of interest. J_{kj} is the total number of photons emitted per second for the k → j transition from the length of the line source viewed by the monochromator.

Two major corrections must be made in equation (23) prior to its use in determining absolute conversion efficiencies. The signal strength, $S_i(\bar{\lambda}_i)$, must be corrected for background radiation from the scintillation cell, and $S_i'(\bar{\lambda}_i)$ must be corrected for scattered light from the tungsten lamp. Figure 19 shows the averaged result of two scans of the KrF* feature at 2487 Å. The data have been divided channel by channel by the average of the two beam current scans taken with the data scans. Each channel in Figure 19 represents some number of counts per unit beam current. An average background, $\bar{N}$, was determined as indicated in Figure 19. This background was subtracted channel by channel over an appropriate channel

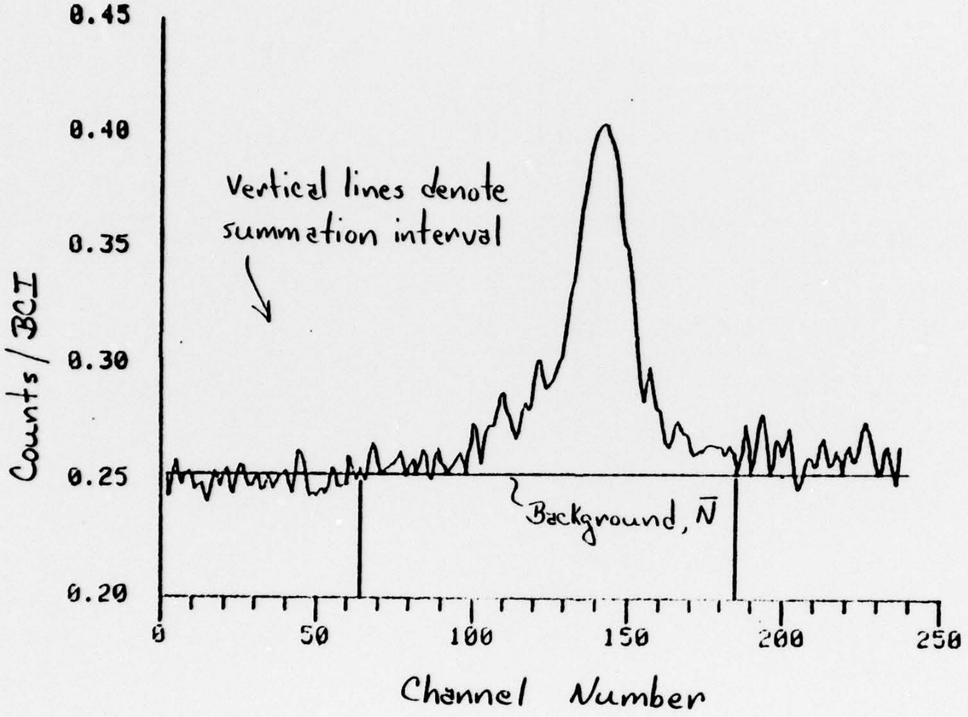

Figure 19 : Absolute Calibration Data. Scan of XeF Feature. The spectrum shown here is an average of two scans of the XeF feature. The number of counts in each channel has been divided by the number of beam current pulses per channel from MCA #2 (see Figure 4).

number interval, and the results were summed to obtain the true number of photons counted.

The correction made for the scattered light from the calibration lamp was performed using techniques discussed by Van den Bos et. al.[19] This method involves using two filters. One is a slot transmission filter for the wavelength region of interest. This filter is present in the optical system during scans of both the tungsten lamp and the scintillation cell. The transmission curve for this slot filter is shown in Figure 20. The tungsten lamp emits strongly in the red region, and, as can be seen in Figure 20, much of this radiation will be passed by the slot filter. This transmitted radiation is the primary source of scattered light in the monochromater, and the scattered light signal tends to obscure the true u.v. signal from the lamp.

A second filter was used to correct the lamp scans for the scattered light signal. This filter was a piece of plexiglass whose transmission curve is shown in Figure 21. The plexiglass filter does not pass radiation in the ultraviolet region. Therefore, a scan of the lamp with both filters in place gives a signal strength which can be subtracted channel by channel from a scan with only the slot filter in place. The resulting spectrum will have been corrected for scattered light in the monochromator. The plexiglass filter is not perfect, and some absorption and reflection occur for the visible wavelength region. A correction factor, γ, was computed by comparing the transmission of the plexiglass-slot filter combination to the transmission of the slot filter alone.

$$\gamma = \frac{\int_\lambda E(\lambda)\ T_o(\lambda)\ d\lambda}{\int_\lambda E(\lambda)\ T_o(\lambda) T_1(\lambda) d\lambda}\ , \quad (\gamma > 1) \qquad (24)$$

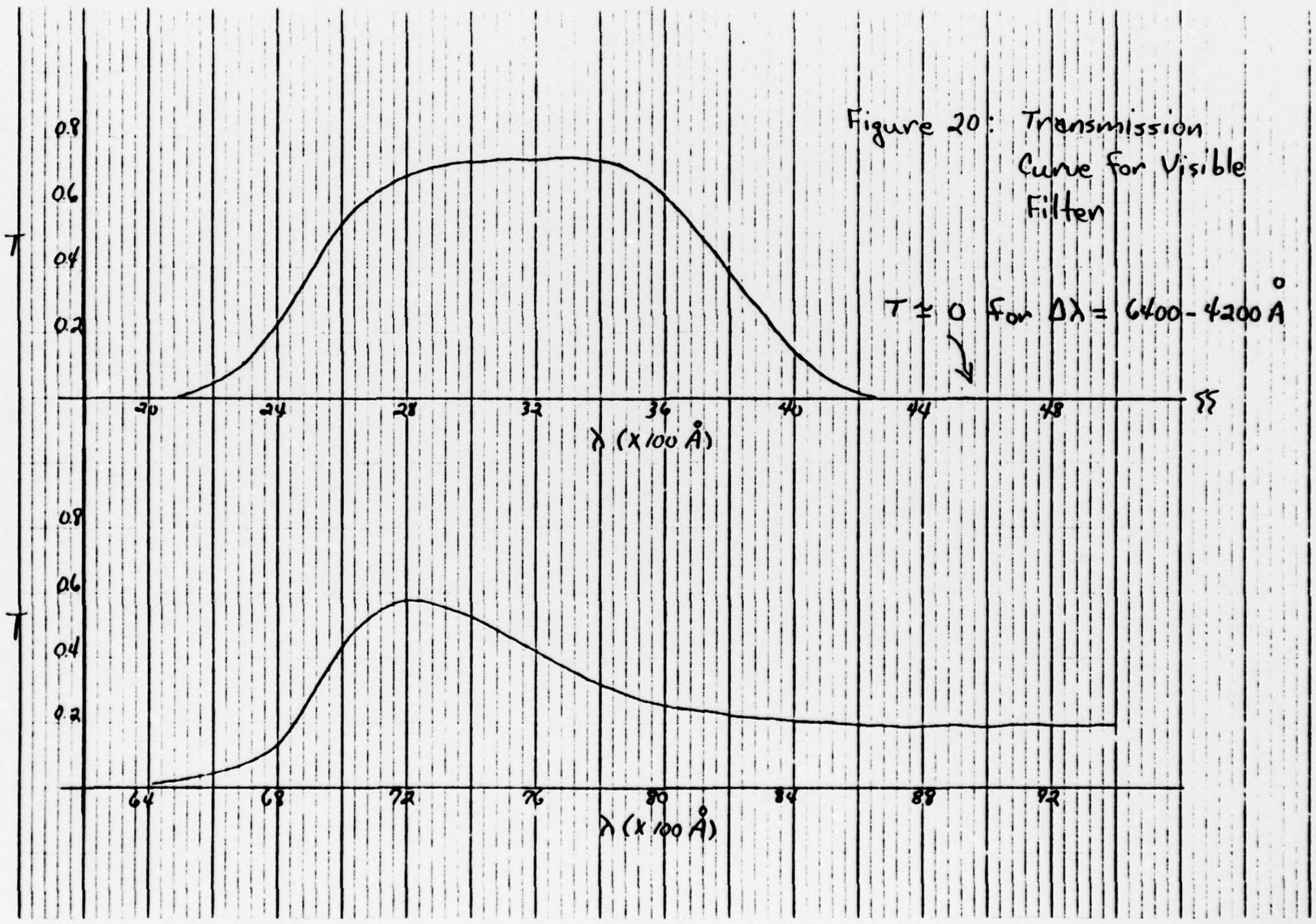

Figure 20: Transmission Curve for Visible Filter

$T \simeq 0$ for $\Delta\lambda = 6400 - 4200$ Å

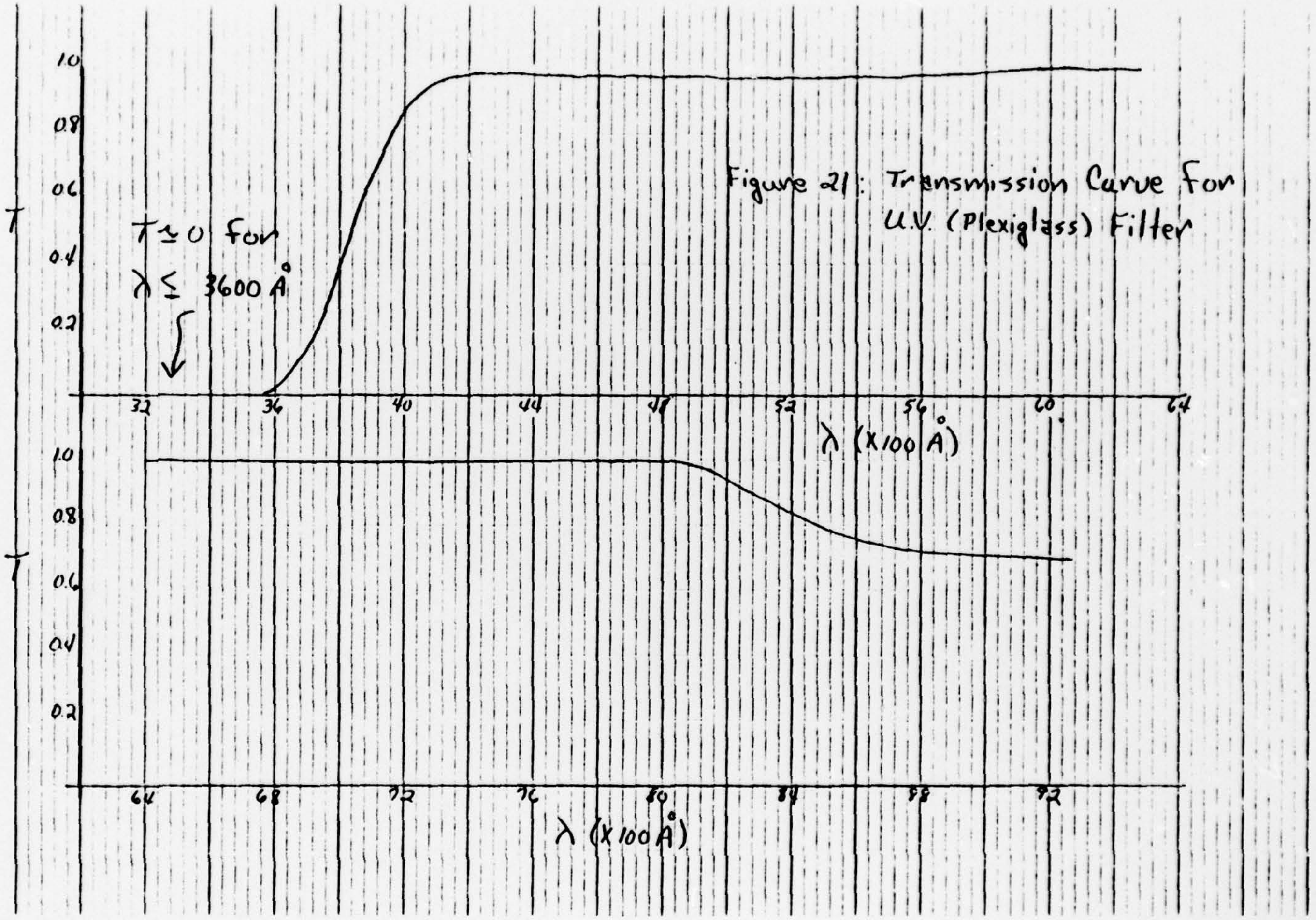

Figure 21: Transmission Curve for U.V. (Plexiglass) Filter

where $E(\lambda)$ is the emissivity of the tungsten lamp, and $T_o(\lambda)$ and $T_1(\lambda)$ are the transmissions of the slot filter and the plexiglass filter, respectively. γ was approximately 1.19 for our calibration procedure.

Equation (23) can now be written as

$$J_{kj} = 4\pi R^2 \Delta\lambda \sum_{i=1}^{N} E(\bar{\lambda}_i) \left[\frac{S_i(\bar{\lambda}_i) - \bar{N}}{S'_{i0}(\bar{\lambda}_i) - \gamma S'_{i1}(\bar{\lambda}_i)} \right] \qquad (25)$$

where $S'_{i0}(\bar{\lambda}_i)$ corresponds to a lamp scan with only the slot filter in place, and $S'_{i1}(\bar{\lambda}_i)$ is a similar scan with both the slot filter and the plexiglass filter in place. J_{kj} is the total number of photons emitted per second per unit beam current from the line source (length = 2.63 cm) viewed by the monochromator. The total photon energy is determined by multiplying equation (25) by $hc/\bar{\lambda}_i$ where h is Planck's constant and c is the speed of light.

$$E_{kj} = 4\pi R^2 hc\Delta\lambda \sum_{i=1}^{N} \frac{E(\bar{\lambda}_i)}{\bar{\lambda}_i} \left[\frac{S_i(\bar{\lambda}_i) - \bar{N}}{S'_{i0}(\bar{\lambda}_i) - \gamma S'_{i1}(\bar{\lambda}_1)} \right] \qquad (26)$$

The quantity, E_{kj}, may be used with the energy deposited in the scintillation cell by the proton beam to calculate absolute conversion efficiencies for a particular gas mixture.

The energy loss calculations for the proton beam were performed using procedures given in reference 16. A 2 MeV proton loses approximately 190 KeV in traversing a 0.1 mil Havar foil. The proton then travels through 3.08 cm of the gas mixture prior to reaching the length of the gas cell viewed by the monochromator. Over this 3.08 cm length the proton loses some additional amount of energy which depends on the total pressure of the gas mixture and the partial pressures of its components. Finally, some energy, ΔE, is deposited by the proton along the length of the cell viewed by the monochromator. This energy loss is computed and used with E_{ij} to determine an absolute conversion efficiency. The following table gives typical energy losses for the gas mixtures studied in this work.

Table 3

$P_{Kr} = 40$ torr
$P_{NF_3} = 2$ torr

$\Delta E = 190$ KeV for a 2 MeV proton transversing a 0.1 mil Havar foil

P_{uf_6} (torr)	E_p(MeV) after 3.08 cm	E_p(KeV) for next 2.63 cm
0	1.7665	38.105
0.1	1.7661	38.500
0.2	1.7656	38.894
0.5	1.7643	40.080
1.0	1.7620	42.059
2.0	1.7575	46.030

Recall that our calibration procedure allows us to compute an absolute conversion efficiency for the $P_{UF_6} = 0$ torr point on each of the relative intensity curves shown in Figures 15 and 16. Therefore, an absolute efficiency can be computed for each of the remaining points by using the relative intensity data and energy loss values similar to those given in Table 3. Results for the Kr - NF_3, Xe - NF_3, Kr - NF_3 - UF_6, and Xe - NF_3 - UF_6 systems are shown in Figures 22 and 23. The data presented in these two figures have been corrected for the difference in energy deposition caused by the varying NF_3 and UF_6 partial presurres. Therefore, comparison of any two points on one of the curves may be made under conditions of equal energy deposition for both points.

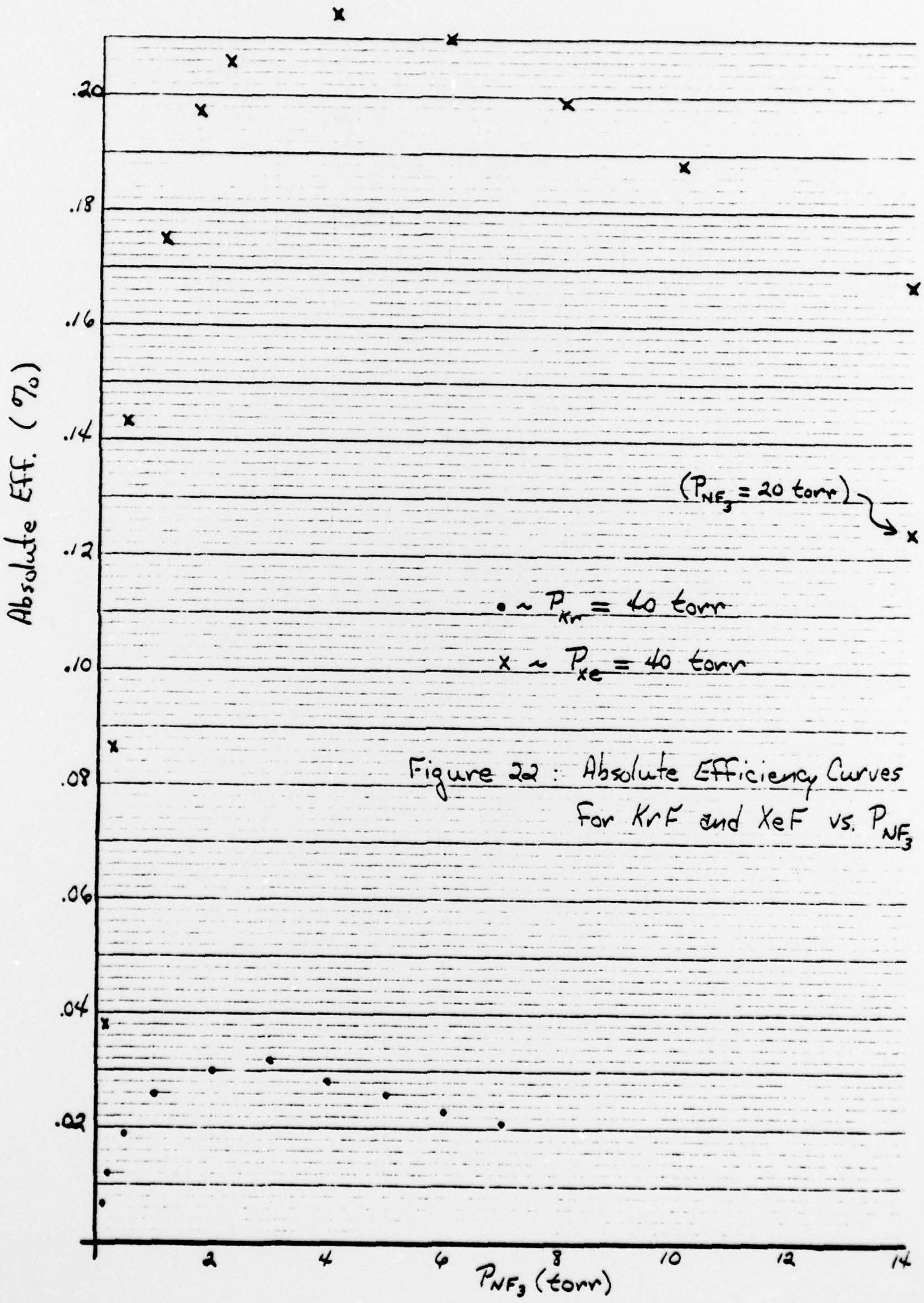

Figure 22 : Absolute Efficiency Curves For KrF and XeF vs. P_{NF_3}

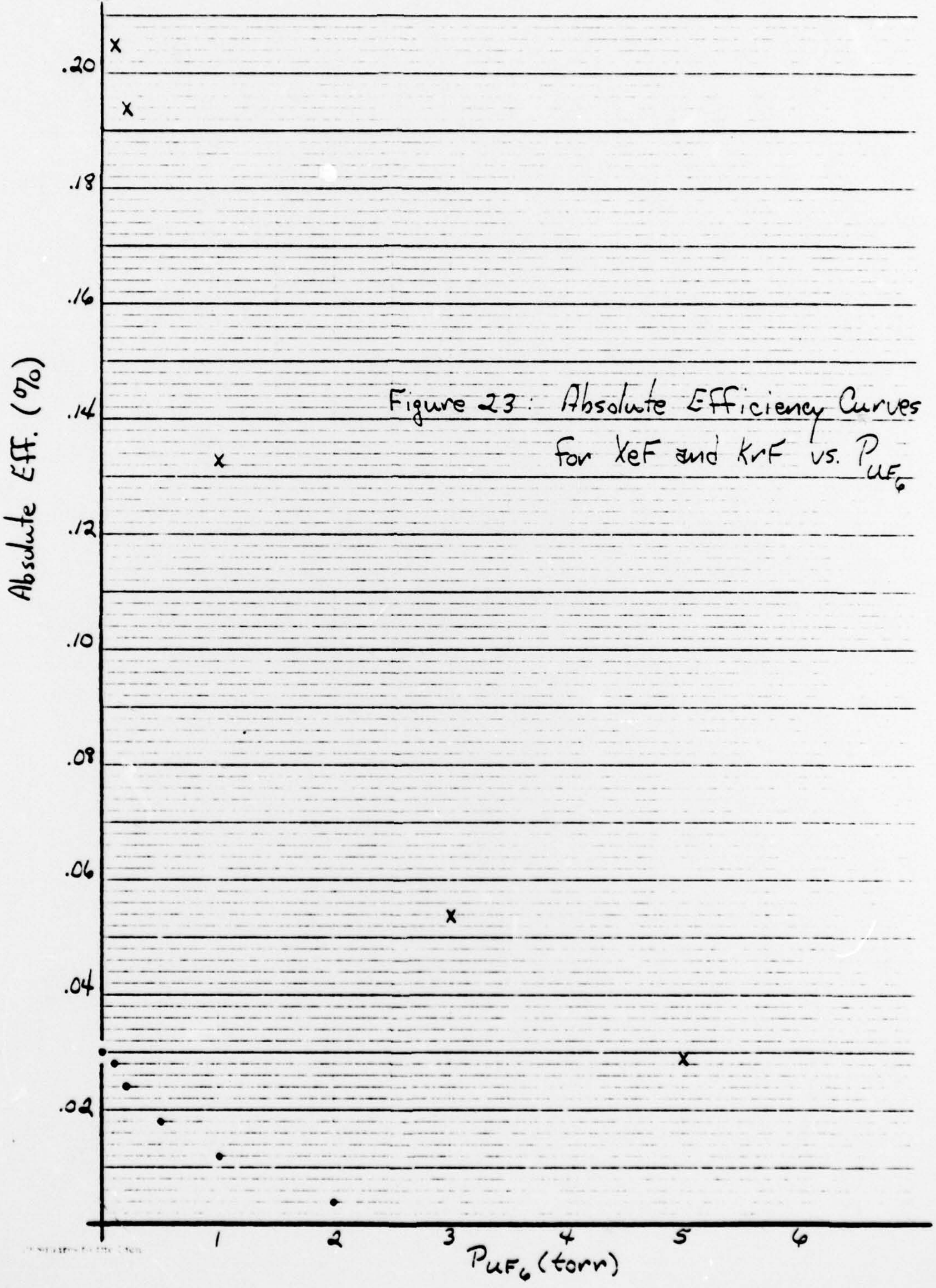

Figure 23: Absolute Efficiency Curves for XeF and KrF vs. P_{UF_6}

V. Conclusions

The Dynamitron particle accelerator (Section II A) together with the single photon counting system described in Section II C serve as a powerful tool for the determination of basic parameter information for atomic and molecular states in gas mixtures. The formation rate constants, K_1, for the reactions

$$Kr^* + NF_3 \xrightarrow{K_1} KrF^* + NF_2$$

and

$$Xe^* + NF_3 \xrightarrow{K_1} XeF^* + NF_2$$

given in Table 1 have not been previously reported in the literature. These rate constants have been determined from experimental data using an analysis technique proposed by E. R. Fisher et. al.[14] This technique involves consideration of only the metastable reaction channel (i.e. the ion channel is neglected) when a rare gas-halide system is experimentally investigated under conditions of low energy deposition and low total pressure. The agreement between our experimental results and the Wayne State calculations is good. However, these calculations point to one significant problem with the Dynamitron accelerator. The machine is not capable of providing the high energy deposition rates for which the ion reaction channel becomes important. Ideally, NPL systems should operate under conditions of high total pressure and high energy deposition rates. Here, the ion channel dominates so that accurate simulation may not be possible with a low intensity particle accelerator. A second proposal which deals with the construction of an intense, pulsed proton source is being considered by BMDATC at the present time. This intense proton source should provide energy deposition rates which more accurately simulate an NPL environment.

The results of the absolute intensity measurements show the Xe-NF_3 system to be the more efficient of the two systems, Xe-NF_3 and Kr-NF_3. However, we must remember that these conversion efficiencies have been measured under conditions where the metastable reaction channel dominates in the formation of XeF^* and KrF^*. The conversion efficiency results for XeF are believed accurate to within ± 50%. The KrF conversion efficiencies are probably less accurate than the XeF efficiencies because of greater uncertainty in the emissivity of the tungsten lamp in the 2487 Å wavelength region (λ = 3525 Å for XeF). Improvements in the efficiency measurements could possibly be achieved by using a different calibration standard (e.g. a deuterium lamp) for the KrF measurements and also by performing more accurate calculations for the proton energy deposition in the gas cell. Empirical relations[10] have been used for this work, and these calculations are considered less accurate than energy loss calculations of the type described in reference 13.

Finally, UF_6 does not appear to be a good fluorine donor for rare gas-halide laser systems. Primarily, this results from the large optical absorption cross section exhibited by UF_6 in the 2000-4000 Å wavelength region. The XeF^* emission occurs at 3525 Å, and here the UF_6 absorption cross section is smaller than at most other wavelengths (see Figure 17). However, results from the present work indicate that XeF^* emission from a low pressure Xe-NF_3 mixture is collisionally quenched when small amounts of UF_6 are added. Attempts will be made in the future to determine the magnitude of the quenching rate constant. At the present time this rate constant appears to be quite large.

REFERENCES

1. M. Rokni, J. A. Mangano, J. H. Jacob, and J. C. Hsia, IEEE J. Quantum Electronics, Vol. Qe-14, (7), p. 464, July, 1978.
2. W. L. Nighan, IEEE J. Quantum Electronics, Vol. QE-14, (10), p.714, Oct., 1978.
3. G. H. Miley, U. S. Army Ballistic Missile Defense Advanced Technology Center, Redstone Arsenal, AL, Contract # DASG60-77-C-0130.
4. J. G. Eden, R. W. Waynant, S. K. Searles, and R. Burnham, Appl. Phys. Lett., Vol. 32, p. 733, 1978.
5. H. C. Brashears, Jr., D. W. Setser, and D. DesMarteau, Chem. Phys. Lett., Vol. 48, p. 84, 1977.
6. J. H. Jacob, M. Rokni, J. A. Mangano, and R. Brochou, Appl. Phys. Lett., p. 109, Jan., 1978.
7. M. Rokni, J. H. Jacob, J. A. Mangano, and R. Brochou, Appl. Phys. Lett., Vol. 30, p. 458, 1977.
8. J. E. Velasco, J. H. Kolts, and D. W. Setser, J. Chem. Phys. 69 (10), p. 4357, 1978.
9. ORTEC: Ion and Plasma Physics Systems, 1 July 1969, and references contained therein.
10. T. G. Miller, J. R. Williams, D. Womack, M. Monahan, and Q. C. Murphree, Rev. Sci. Instr., accepted for publication, Apr., 1978.
11. J. L. Mack and G. B. Wilmot, Rev. Sci. Instr. 36, 1265, (1965).
12. C. H. Chen, M. G. Payne, G. S. Hurst, and J. P. Judish, J. Chem. Phys. 65, 4028 (1976).
13. E. R. Fisher and S. S. Lim, U. S. Army Ballistic Missile Defense Advanced Technology Center, Redstone Arsenal, AL, Contract # DASG60-78-0055.

14. E. R. Fisher, Wayne State University, Detroit, MI, private communication.

15. C. Chen and M. G. Payne, IEEE J. Quantum Electronics, Vol. QE-15, (3), p. 149, Mar., 1979.

16. L. C. Northcliffe and R. F. Schilling, Nuclear Data Tables, A7, p. 233, 1970.

17. E. W. Thomas, Excitation in Heavy Particle Collisions, John Wiley and Sons, p. 47, 1972.

18. M. Monahan, M. S. Thesis, Auburn University, June, 1979, in preparation.

19. J. Van Den Bos, G. J. Winter, and F. J. DeHeer, Physica, 40, p. 357 (1968).